ENGINEERING PERSPECTIVE

CONTENTS

ENGINEERING PERSPECTIVE Volume: 1 Issue: 1 31 March 2021

e-ISSN: 2757-9077

Open Access

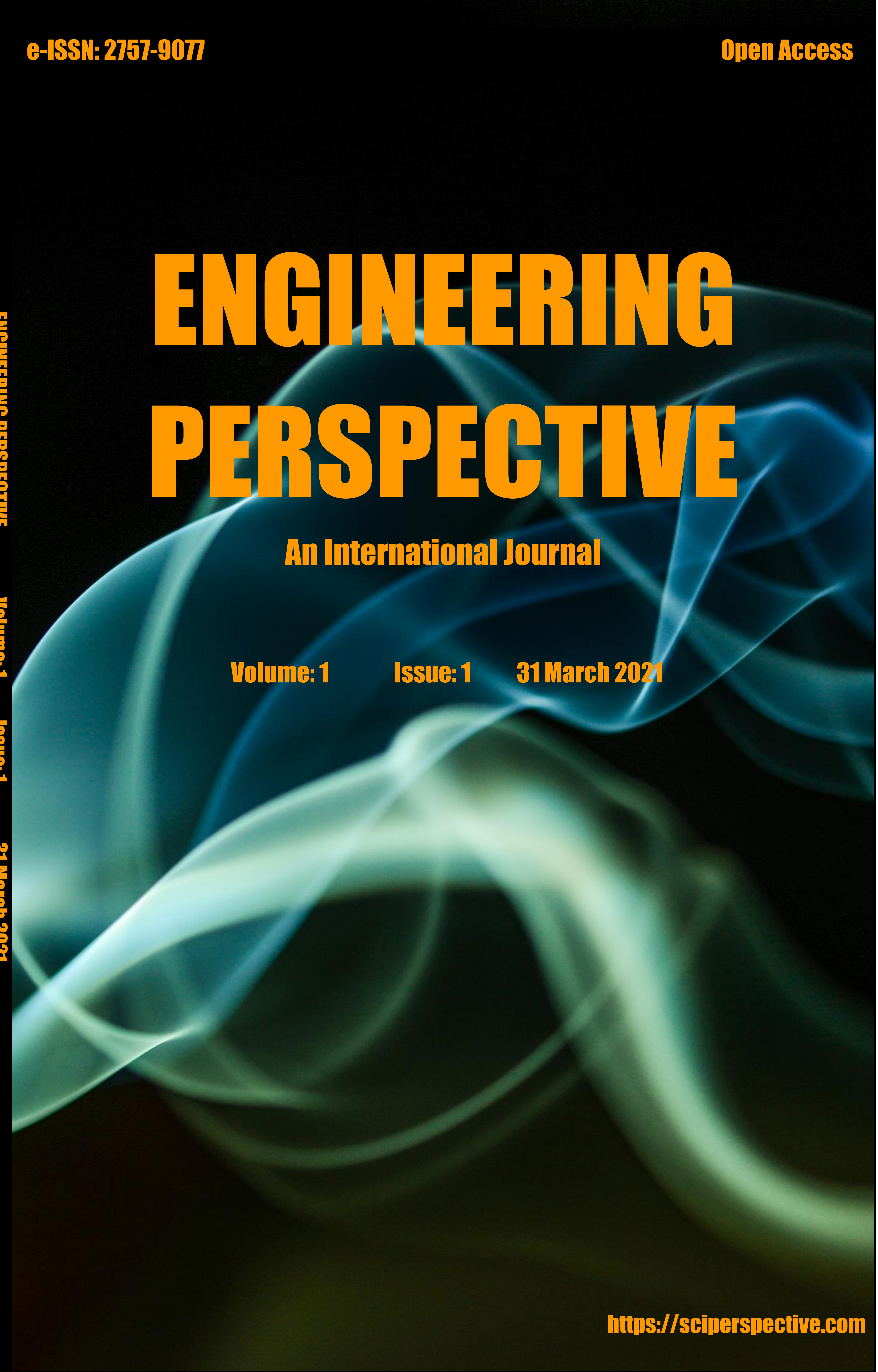

ENGINEERING PERSPECTIVE

An International Journal

Volume: 1 Issue: 1 31 March 2021

https://sciperspective.com

Engineering Perspective 1 (1): 1-5, 2021

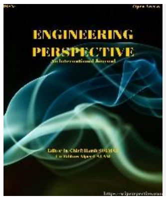

e-ISSN:2757-9077

ENGINEERING PERSPECTIVE

https://sciperspective.com/

Research Paper

Electrochemical Behavior and Voltammetric Determination of 2-Nitrophenol on Glassy Carbon Electrode Surface Modified with 1-Amino-2-Naphthol-4-Sulphonic Acid

Tuğba Tabanlıgil Calam[1*]

[1] *Technical Sciences Vocational High School, Gazi University, Ankara, 06374, Turkey*

Abstract

2NP is among the priority pollutants for the environmental ecosystem and poses a threat to the health of living things by mixing in wastewater. Therefore, the 2NP determination is important. In this study, the glassy carbon (GC) electrode surface was modified with 1-amino-2-naphthol-4-sulfonic acid (ANSA). The electrochemical behavior and voltammetric determination of 2-nitrophenol (2NP) on the modified surface (ANSA-GC) was performed. Firstly, it was decided that the supporting electrolyte medium suitable for 2NP determination was Britton-Robinson (BR) buffer and the effect of pH change on the reduction peak of 2NP in this environment was investigated. The effect of changing scan rate on the reduction peak of 2NP was examined and this study showed that the reduction process of 2NP on the ANSA-GC modified electrode surface was diffusion controlled process. For 2NP determination,two linear working ranges with two different slopes, 1.19×10^{-6}-1.66×10^{-4} M and 1.66×10^{-4}-1.14×10^{-3} M were obtained. LOD and LOQ values were calculated as 0.29 µM and 0.97 µM, respectively. Finally, lake water was used as the real sample, and 2NP was determined in this lake water. The experimental results showed that it can be used with a high accuracy and precision in the determination of 2NP with ANSA-GC modified electrode.

Keywords: Voltammetric determination; modification; electrode; 2-nitrophenol; toxic

History
Received: 23.12.2020
Accepted: 21.03.2021

Author Contacts
**Corresponding Author*
ttabanligil@gazi.edu.tr
Orcid: 0000-0002-3712-7713

http://dx.doi.org/10.29228/sciperspective.48525

1. Introduction

Nitrophenols are widely used as reagents for pesticide, herbicide and explosive production, and as intermediates in dye synthesis [1,2]. These organic compounds are considered by the US Environmental Protection Agency (USEPA) as one of the primary toxic pollutants. 2-nitrophenol (2NP) is among the most toxic and persistent organic pollutants of industrial wastewater. USEPA lists 2NP as "priority pollutant" [3]. 2NP shows high toxicity and/or mutagenicity to many living organisms, directly or through some of its catabolic metabolites [4].

It is important to determine nitrophenols, especially 2NP, with an exact and reliable method due to its negative effects on the ecosystem and living health. In the literature, there are determinations of nitrophenols using methods such as spectrophotometry [5] fluorescence [6] gas chromatography [7] capillary electrophoresis [8] and high-performance liquid chromatography [9]. However, these methods are costly and time consuming, as these methods have many processing steps and require pre-treatment. In addition, the cost of the devices needed for these methods is another disadvantage. On the other hand, electrochemical methods have useful features such as low cost, ease of use, short response time, portable simple devices and high sensitivity and selectivity. For this reason, the determination of 2NP made by electrochemical methods are preferred [10-12].

In this study, an alternative detection method for 2NP determination has been developed. The electrochemical behavior of 2NP was examined with the sensor prepared for this purpose. In order to examine the analytical performance of the sensor for 2NP determination, parameters such as linear working range and detection limit were figured out. Finally, the 2NP determination in lake water was successfully carried out to show the applicability of the sensor in real sample.

2. Experimental Method

2.1 Chemicals

All chemicals were of analytical reagent grade. ANSA, 2NP, phosphoric acid, potassium chloride (KCl) used in the study were purchased from Sigma-Aldrich. Sodium acetate, acetic acid (glacial), sodium phosphate monobasic, sodium phosphate dibasic, boric acid and sodium hydroxide were purchased from Merck.

The stock solution of 2NP was prepared at a concentration of 1×10^{-2} M using ultrapure water. The 1×10^{-4} M ANSA solution in the presence of 0.1 M KCl solution was used for coating the GC electrode.

2.2. Electrochemical Measurements

Electrochemical experiments were carried out using a computer-controlled potentiostat (CHI brand, 660B model) with a three-electrode system. GC electrode (BAS, MF-2012, geometric area 0.071 cm^2) as working electrode, platinum wire as counter electrode (BAS, MW-1032) and Ag/AgCl/KCl(sat.) as reference electrode (BAS, MF-2052) were used. Cyclic voltammery (CV) and differential pulse voltammery (DPV) techniques were used in electrochemical measurements. The ultrasonic bath used in cleaning the electrode surfaces was the Bandelin brand Sonatax super model. The digital pH meter used for pH adjustments of the prepared solutions was Thermo branded Orion 5 Star model.

2.3. Electrochemical Techniques

The CV technique was used for the modification of GC electrode surfaces with ANSA molecule. This process was carried out for 20 cycles between -1.5 V and 2 V and at a scan rate of 100 mVs^{-1} (vs Ag/AgCl(KCl sat.)). DPV technique was used to examine the electrochemical behavior of 2NP on the ANSA-GC modified electrode surface. In this technique, the amplitude was 0.05 V, the pulse width was 0.05 s, and the pulse period was 0.2 s.

3. Results and Discussion

3.1. Preparation of ANSA-GC modified electrode

Before the modification process, the surfaces of the GC electrodes were cleaned. In the cleaning process, GC electrode surfaces were polished with 0.1 and 0.05 micron alumina suspensions and cleaning pad, respectively. Afterwards, these were sonicated in pure water for 15 minutes and rinsed with pure water. The cleaned GC electrodes were immersed in 1×10^{-4} M ANSA solution prepared in 0.1 M KCl. The ANSA film was deposited on the GC electrode surface using the CV technique between -1.5 V and 2 V and at a scan rate of 100 mVs^{-1} (vs. Ag/AgCl(KCl sat.)) for 20 cycles. The multi-cyclic voltammograms (CVs) obtained were shown in Figure 1. Reduction peaks of ANSA were seen at -0.7 V and +0.2 V, and the peak currents increase with the increase in the number of cycles. The current of the oxidation peak obtained in the first cycle at about 0.1 V did not change current value with the increase in the number of cycles. From the tenth cycle, a shoulder-shaped oxidation peak was observed at approximately +1.4 V with increasing number of cycles.

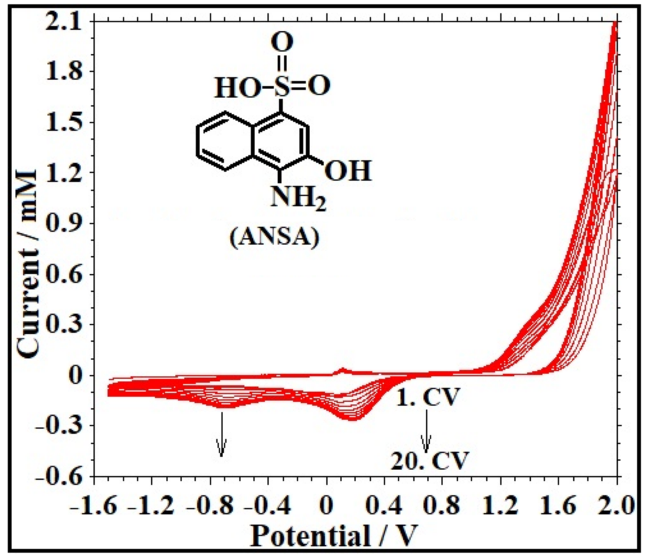

Figure 1. Multiple cyclic voltammogram showing the electrochemical deposition of 1×10^{-4} M ANSA prepared with 0.1 M KCl solution on the GC electrode surface.

3.2. The effect of support electrolyte and its pH on the reduction peak of 2NP

The supporting electrolyte's type and its pH values influence the potential and current of the redox peaks of the analytes [13]. To examine the effect of the supporting electrolyte type on the reduction peak of 2NP, Britton-Robinson buffer (BR) pH 2.0 and pH 6.0, phosphate buffer pH 4.5 and pH 7.0 (PBS), pH 4.5 acetic acid/acetate (HAc/NaAc) buffer and pH 2.0 H_3PO_4 solution were used. The reduction peaks of 2×10^{-4} M 2NP in these solutions were shown in Figure 2A. The cathodic peak currents of 2NP in these medias were obtained 19.55 µM, 7.99 µM, 14.71 µM, 8.079 µM, 14.30 µM and 17.26 µM, respectively. The cathodic peak current was found to be high in acidic medias, and the highest peak current was obtained in pH 2.0 BR buffer media. Therefore, 2NP determination with ANSA-GC electrode was found appropriate in BR buffer solution.

In order to examine the effect of the change in the pH value of the support electrolyte media on the cathodic peak of 2NP, the reduction peaks of 2×10^{-4} M 2NP in BR buffer solutions prepared with pH values of 1.0, 2.0, 3.0, 4.0, 5.0 and 6.0 were obtained and shown in Figure 2B. Figure 2C showed the peak potential and peak current change with pH value. The highest cathodic peak current of 2NP was obtained in pH 2.0 BR buffer solution. After pH 2.0, it was observed that the peak current decreased as the pH value increased. For this reason, it was decided that the support electrolyte medium suitable for the determination of 2NP with ANSA-GC electrode was pH 2.0 BR buffer. The relationship between pH and potential was obtained by the equation E(V)= -0.0574pH-0.4840 (R^2=0.9990). This case showed that the reduction of 2NP was directly related to protons. Using the Nernst equation [14] known as dEp/dpH = 2.303mRT/nF, the value of "m/n" was calculated to be 0.97 (approximately 1). This result showed that the number of electrons and protons were equal in the reduction of 2NP. In Nernst equation, T is the temperature (298.15 K), R is the gas constant (8.314 $JK^{-1}mol^{-1}$), F is the faraday constant (96485 C mol^{-1}), m and n are the numbers of protons and electrons, respectively.

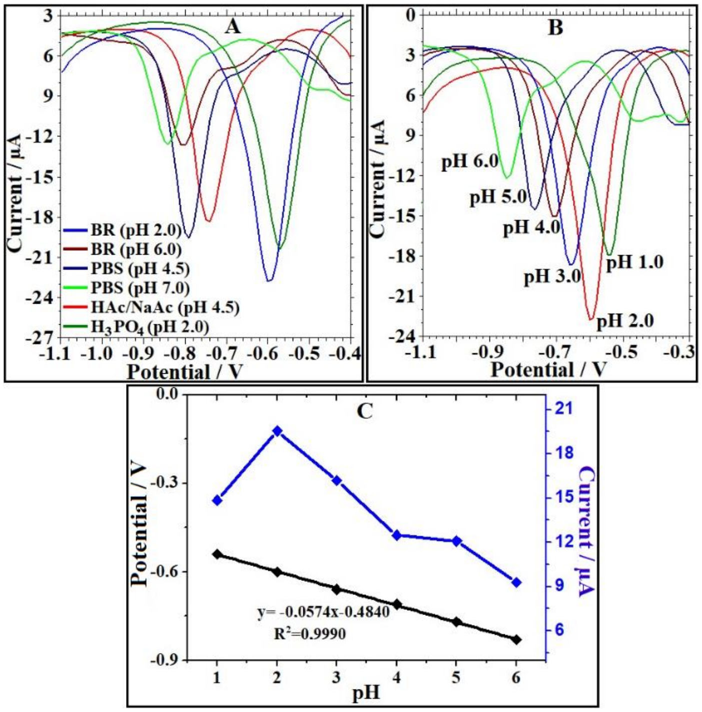

Figure 2. DPVs of 2×10^{-4} M 2NP in different support electrolyte medias (A), DPVs of 2×10^{-4} M 2NP in different pH values of BR buffer (B), Plot of reduction peak current and potential values of 2×10^{-4} M 2NP versus pH values of BR buffer (C).

3.3. The effect of scan rate on the cathodic peak of 2NP

CVs of 2×10^{-4} M 2NP were obtained at scan rates varying between 10-400 mVs^{-1} and were shown in Figure 3A. According to the changing scan rate values, the cathodic peak current values of 2NP were given in Figure 3B and it was seen that the graph was not linear. This case showed that the reduction process of 2NP was diffusion controlled [15]. In Figure 3C, Ipc graph against $\nu^{1/2}$ was given. The equation of this graph obtained linearly is Ipc (µA) = $25.427\nu^{1/2}$ $(Vs^{-1})^{1/2}$ +1.367 (R^2=0.9994). The linearity of this graph also showed that the reduction process of 2NP was diffusion controlled [17-19]. In addition, the slope value of the logIpc graph (Figure 3D) drawn with respect to logν was obtained as 0.4085. The fact that this value was close to the theoretical value of 0.5 also confirms that the process was diffusion controlled [15, 16].

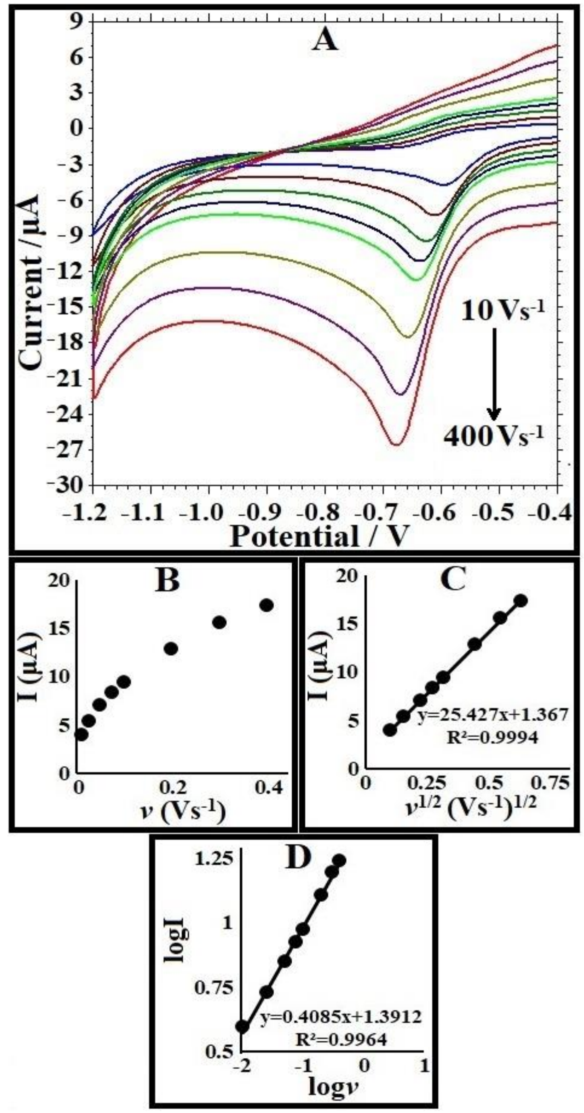

Figure 3. A. CVs of 2×10^{-4} M 2NP taken at 10, 25, 50, 75, 100, 200, 300 and 400 mVs^{-1} scan rate on the ANSA-GC modified electrode surface, B. Ipc versus ν, C. Ipc graph against $\nu^{1/2}$, D. Plot of logIpc versus logν.

3.4. Determination of working range, LOD and LOQ values

2NP additions were made on the support electrolyte to determine the working range of the ANSA-GC modified electrode in the determination of 2NP. Voltammograms and calibration graph were given in Figure 4. A linear working range with two different slopes of 1.19×10^{-6}-1.66×10^{-4} M and 1.66×10^{-4}-1.14×10^{-3} M were obtained. LOD and LOQ values were calculated as 0.29 and 0.97 µM, respectively. LOD and LOQ were calculated using the formulas 3*S*/m and 10*S*/m, respectively, with the standard deviation value of *S* and the slope value of m [16].

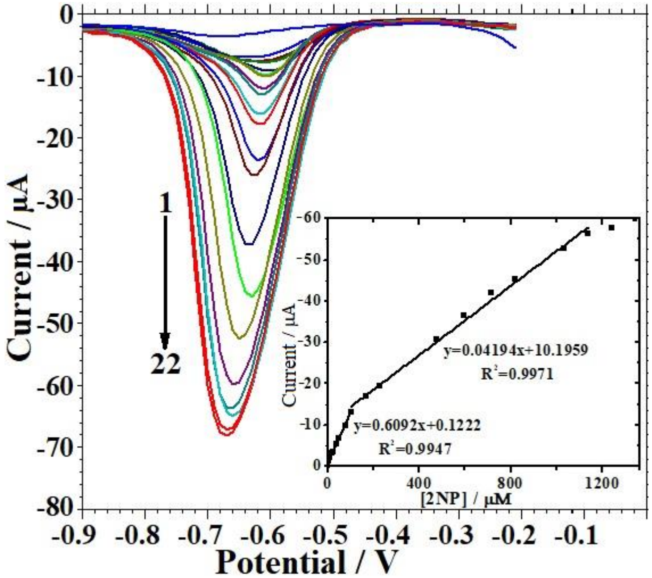

Figure 4. DPVs and calibration graph obtained with ANSA-GC modified electrode by adding 2NP on the support electrolyte. 1 → 22: 0, 1.19, 1.6, 2.64, 3.65, 8.82, 18.67, 24.50, 38.28, 51.67, 77.37, 101.7, 166.6, 230.6, 478.6, 597.9, 714.2, 817.7, 1034.3, 1138.8, 1240.9, 1340.7 µM.

3.5. Repeatability Study

The cathodic peak of 2×10^{-4} M 2NP was obtained with five repeated experiments on the ANSA-GC modified electrode in order to examine the repeatability of the modified electrode. Percent relative standard deviation (RSD%) (*S*/X.100) of the peak currents was calculated as 3.50%. This value showed that the ANSA-GC modified electrode was good repeatability in 2NP determination.

3.6. Determination of 2NP in real sample

Water samples were taken from Mogan Lake in Ankara, Turkey in order to make the actual sample analysis. First, the same volumes of water sample and BR buffer solution were mixed. In order to understand whether there is 2NP in the lake water; DP voltammograms of pH = 2.0 BR buffer and lake water sample mixture were obtained. Obtaining almost the same voltammogram for these two samples showed that 2NP was not found in lake water. For this reason, 2NP was added to the lake water sample at a concentration of 10 µM, and then 2NP additions were continued and the determination was carried out using the standard addition method. The use of the DPV technique in the quantitative determination of 2-NP in real samples by electrochemical methods is quite common [20-23]. Voltammograms obtained are given in Figure 5. In the results of the experiments repeated three times, the % RSD related to the repeatability and the % Bias values related to the accuracy of the method were obtained as 1.51 and 3.8, respectively. These values showed that the reproducibility and accuracy of 2NP determination with the proposed method is good.

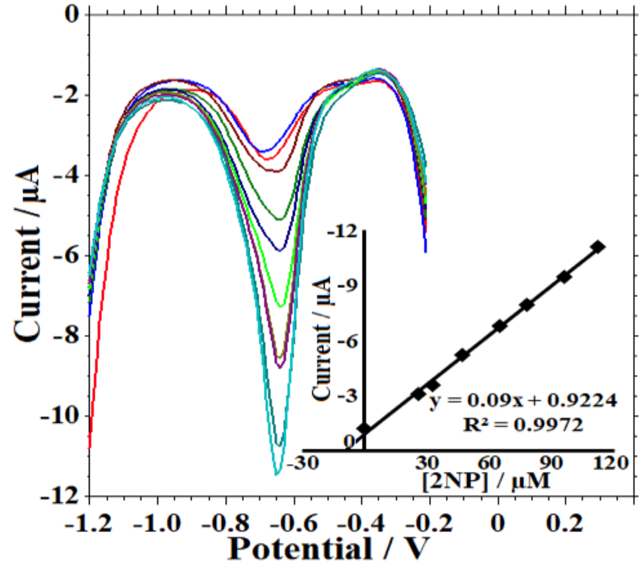

Figure 5. DPVs obtained with 2NP additions in lake water sample and calibration graph (1) pH 2.0 BR buffer (2) Lake water sample, (3) 2NP addition (determined 10 µM 2NP), (4) 26 µM, (5) 33 µM, (6) 47 µM, (7) 65 µM, (8) 78 µM, (9) 96 µM, and (10) 112 µM 2NP.

4. Conclusion

In this study, the GC electrode surface was modified with 1-amino-2-naphthol-4-sulfonic acid molecule. The 2NP determination was successfully performed with the prepared sensor (ANSA-GC). The sensor showed a wide linear working range for 2NP determination. In addition, the modification process of ANSA-GC electrode was extremely simple and fast. With the ANSA-GC electrode, 2NP determination was provided with high sensitivity, short measurement time, repeatability, high accuracy and good analytical performance. In addition, the determination of 2NP in lake water was successfully performed by using ANSA-GC electrode.

This is the extended version of the study presented on 3rd ERASMUS International Academic Research Symposium (March, 2020).

Conflict of Interest Statement

The author declares that there is no conflict of interest

References

1. Alif, A., & Boule, P. (1991). Photochemistry and environment Part XIV. Phototransformation of nitrophenols induced by excitation of nitrite and nitrate ions. Journal of Photochemistry and Photobiology A: Chemistry, 59(3), 357-367.
2. Takahashi, N., Nakai, T., Satoh, Y., & Katoh, Y. (1994). Variation of biodegradability of nitrogenous organic compounds by ozonation. Water Research, 28(7), 1563-1570.
3. U.S. Environmental Protection Agency, Health and Environmental Effects, Ambient Water Quality Criteria for Nitrophenols. EPA 440/5-80-063, Washington, DC (1980).

4. Roldan, M. D., Blasco, R., Caballero, F. J., & Castillo, F. (1997). Degradation of p-nitrophenol by the phototrophic bacterium Rhodobacter capsulatus. Archives of microbiology, 169(1), 36-42.
5. Niazi, A., & Yazdanipour, A. (2007). Spectrophotometric simultaneous determination of nitrophenol isomers by orthogonal signal correction and partial least squares. Journal of hazardous materials, 146(1-2), 421-427.
6. Zhang, W., Wilson, C. R., & Danielson, N. D. (2008). Indirect fluorescent determination of selected nitro-aromatic and pharmaceutical compounds via UV-photolysis of 2-phenylbenzimidazole-5-sulfonate. Talanta, 74(5), 1400-1407.
7. Padilla-Sánchez, J. A., Plaza-Bolaños, P., Romero-González, R., Garrido-Frenich, A., & Vidal, J. L. M. (2010). Application of a quick, easy, cheap, effective, rugged and safe-based method for the simultaneous extraction of chlorophenols, alkylphenols, nitrophenols and cresols in agricultural soils, analyzed by using gas chromatography–triple quadrupole-mass spectrometry/mass spectrometry. Journal of Chromatography A, 1217(36), 5724-5731.
8. Guo, X., Wang, Z., & Zhou, S. (2004). The separation and determination of nitrophenol isomers by high-performance capillary zone electrophoresis. Talanta, 64(1), 135-139.
9. Hofmann, D., Hartmann, F., & Herrmann, H. (2008). Analysis of nitrophenols in cloud water with a miniaturized light-phase rotary perforator and HPLC-MS. Analytical and bioanalytical chemistry, 391(1), 161-169.
10. Liu, J., Chen, Y., Guo, Y., Yang, F., & Cheng, F. (2013). Electrochemical sensor for o-nitrophenol based on β-cyclodextrin functionalized graphene nanosheets. Journal of Nanomaterials, 2013.
11. Luo, L. Q., Zou, X. L., Ding, Y. P., & Wu, Q. S. (2008). Derivative voltammetric direct simultaneous determination of nitrophenol isomers at a carbon nanotube modified electrode. Sensors and Actuators B: Chemical, 135(1), 61-65.
12. Baysal, G., Uzun, D., & Hasdemir, E. (2020). The fabrication of a new modified pencil graphite electrode for the electrocatalytic reduction of 2-nitrophenol in water samples. Journal of Electroanalytical Chemistry, 860, 113893.
13. Uzun, D., Gündüzalp, A. B., & Hasdemir, E. (2015). Selective determination of dopamine in the presence of uric acid and ascorbic acid by N, N′-bis (indole-3-carboxaldimine)-1, 2-diaminocyclohexane thin film modified glassy carbon electrode by differential pulse voltammetry. Journal of Electroanalytical Chemistry, 747, 68-76.
14. Calam, T. T., & Uzun, D. (2019). Rapid and Selective Determination of Vanillin in the Presence of Caffeine, its Electrochemical Behavior on an Au Electrode Electropolymerized with 3-amino-1, 2, 4-triazole-5-thiol. Electroanalysis, 31(12), 2347-2358.
15. Tabanlıgil Calam, T. Elektropolimerize 3, 5-Diamino-1, 2, 4-triazol Film ile Modifiye Edilmiş Altın Elektrot Yüzeyinde Epinefrinin Voltammetrik Tayini ve Elektrokimyasal Davranışı. Gazi Üniversitesi Fen Bilimleri Dergisi Part C: Tasarım ve Teknoloji, 7(4), 985-998.
16. Brycht, M., Özmen, T., Burnat, B., Kaczmarska, K., Leniart, A., Taştekin, M., ... & Skrzypek, S. (2016). Voltammetric behavior, quantitative determination, and corrosion investigation of herbicide bromacil. Journal of Electroanalytical Chemistry, 770, 6-13.
17. Tabanlıgil Calam, T. (2019). Analytical application of the poly (1H-1, 2, 4-triazole-3-thiol) modified gold electrode for high-sensitive voltammetric determination of catechol in tap and lake water samples. International Journal of Environmental Analytical Chemistry, 99(13), 1298-1312.
18. Purushothama, H. T., Nayaka, Y. A., Vinay, M. M., Manjunatha, P., Yathisha, R. O., & Basavarajappa, K. V. (2018). Pencil graphite electrode as an electrochemical sensor for the voltammetric determination of chlorpromazine. Journal of Science: Advanced Materials and Devices, 3(2), 161-166.
19. Barsan, M. M., Pinto, E. M., & Brett, C. M. (2008). Electrosynthesis and electrochemical characterisation of phenazine polymers for application in biosensors. Electrochimica Acta, 53(11), 3973-3982.
20. Capelari, T. B., Pereira, A. C., Gonçalves de Oliveira, L. L., & Teixeira Tarley, C. R. (2019). Sensitive simultaneous determination of o-nitrophenol and p-nitrophenol in water by surfactant-mediated differential pulse voltammetry. *Analytical Letters*, *52*(9), 1462-1476.
21. Birhanzlová-Rumlová, T., Barek, J., Fischer, J., & Vyskočil, V. (2020). Anodic differential pulse voltammetric determination of 2-nitrophenol at a non-traditional carbon film composite electrode. Journal of Electroanalytical Chemistry, 877, 114510.
22. Rodríguez, I. N., Leyva, J. A. M., Hidalgo, J., & de Cisneros, H. (1997). Use of a carbon paste modified electrode for the determination of 2-nitrophenol in a flow system by differential pulse voltammetry. Analytica chimica acta, 344(3), 167-173.
23. Birhanzlová-Rumlová, T., Barek, J., Fischer, J., & Vyskočil, V. (2020). Anodic differential pulse voltammetric determination of 2-nitrophenol at a non-traditional carbon film composite electrode. Journal of Electroanalytical Chemistry, 877, 114510.

Engineering Perspective 1 (1): 6-10, 2021

e-ISSN:2757-9077

ENGINEERING PERSPECTIVE

https://sciperspective.com/

Research Paper

Combustion, Performance and Emissions of Ethanol/n-Heptane Blends in HCCI Engine

Bilal Aydoğan[1*]

[1] *Ship Construction Department, Maritime Voc. High. School, Bandırma Onyedi Eylül University, Balıkesir, 10200, Turkey*

Abstract

The aim of this study was to investigate the effects of the ethanol on combustion, performance and emission characteristics of a single cylinder, port fuel injection HCCI engine was investigated. 15% ethanol and 85% n-heptane were blended. N-heptane was used as reference fuel. The experiments were performed at 1200 rpm and fix inlet air temperature of 60 ºC. The parameters such as in-cylinder pressure, heat release rate, CA50, CA10, ringing intensity, indicated thermal efficiency were detected. Beside this, the emissions of CO and HC were also given in the study. The experimental results showed that E15 didn't significantly effect in-cylinder pressure and heat release rate and there have been slight increase compared to n-heptane. CA50 was retarded about 1.5 ºCA and indicated thermal efficiency increased about 3% with E15 at λ=2.5. Ringing intensity increased about 30% and HC emission decreased with the addition of 15% ethanol and 85% n-heptane fuel

Keywords: Ethanol, combustion, HCCI, performance

History
Received: 24.11.2020
Accepted: 20.03.2021

Author Contacts
**Corresponding Author*
baydogan@bandirma.edu.tr
Orcid: 0000-0002-7928-5867

http://dx.doi.org/10.29228/sciperspective.47890

1. Introduction

In recent years, the energy need in the world has been increasing due to the developing industrialization [1,3]. Similarly, the use of fossil fuels, which meet most of the energy needs, is increasing day by day, but the resources of these fuels are extremely limited. The environmental pollution due to the use of fossil fuels is also a research topic that has been dealing by many researchers. Homogeneous charge compression ignition (HCCI) combustion technology which has high efficiency and very low NO_x and soot formation is one of the alternative combustion concepts [4-10]. Ignition starts spontaneously in the combustion chamber and homogeneous charge burns in HCCI engine. Thereby, the disadvantages of spark ignition engines or diesel engines like flame propagation which affects the autoignition or heterogenitiy can be eliminated by HCCI engines. Besides this, start of combustion can not be directly controlled by any mechanism in HCCI engines [11-17]. So, the problems like misfiring at low loads and knocking at high loads occurs in HCCI combustion [18-21]. There are several methods to solve these problems such as using alternative fuels which has low or high reactivity.

Many researchers have carried out a number of studies which invastigates the effects of alcohols on HCCI combustion. The alcohols like ethanol and methanol are easily accessible, inexpensive and produced from natural sources. Polat [21] performed his experiments at low compression ratio and examined the effects of ethanol in HCCI engine. Ethanol was added into the n-heptane as the ratios of 10, 15 and 20%. The results showed that maximum in-cylinder pressure and heat release rate decreased with increasing the ethanol amount in the mixture. Gawale and Srinivasulu [22] investigated the effects of different mass flow rates of ethanol in HCCI engine at different engine loads. They reported that ignition delay increased with the increase of mass flow rate, however, in-cylinder temperature and pressure reduced. Beside this, NOx and smoke opacity was also reduced owing to low in-cylinder temperature. Taghavifar et al [23] investigated the effects of diesel-DME-methanol blends on combustion in HCCI engine. The experimental results showed that the addition of 20% DME and 30% methanol showed higher pressure and accumulated heat at 1400 rpm. Ghareghani [24] used three fuels, natural gas, ethanol and methanol, in his study and investigated the load limits of HCCI engine. He reported that natural gas is better choice for higher intake temperatured and rich mixtures while ethanol and methanol are good for low intake temperature and lean mixtures. Bendu and Sivalingam [25] invetigated the effects of charge temperature on ethanol fuelled HCCI engine. It was reported that intake air temperature significantly effects the in-cylinder pressure, combustion and thermal efficiency and ringing intensity.

The current study examined, the effects of 15% ethanol (E15) and 85% n-heptane fuel on combustion, performance and emissions in a single cylinder, port fuel injection HCCI engine and compared to n-heptane (H100) reference fuel. For this purpose, in-cylinder pressure, heat release rate, CA10, CA50, indicated thermal efficiency (ITE), ringing intensity (RI), and CO and HC emissions were presented in this paper.

2. Experimental methodology

A single cylinder, port fuel injection HCCI engine which was converted from single cylinder SI engine was used in the experiments. The schematic view of the engine setup and the specifications of the engine were given at Figure 1 and Table 1, respectively.

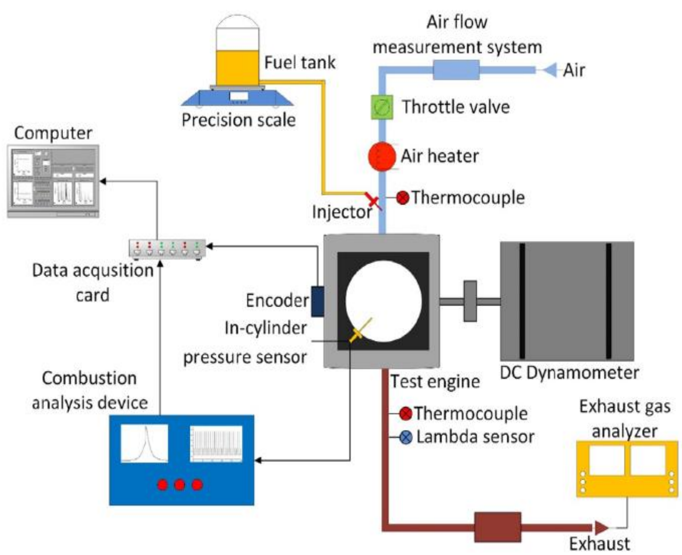

Figure 1. Schematic view of the engine setup

Table 1. The specifications of the engine

Engine model	Ricardo Hydra
Cylinder number	1
Fuel injection system	Port
Bore (mm) x Stroke (mm)	80.26 x 88.90
Compression ratio	13:1
Maximum power outpu (kW)	15

The experiments were performed at 1200 rpm engine speed, 60 ºC and various lambda values (λ=1.7-3.0). DC dynamometer was conducted to the engine and temperatures were measured with K-type thermometer. In-cylinder pressure was quantified with Kristler model 6121 piezoelectric pressure transducer and scaled up by Cussons P4110 analysis device. National Instruments USB 6259 data acquisition card converted the data to digital signals and recorded via the computer. NO, CO emissions and lambda were measured with exhaust gaz analyzer device. Table 2 and 3 shows the technical properties of exhaust gas analyzer and cylinder pressure transducer, respectively. Two fuels were used in the experiments, the first one is as reference fuel n-heptane (H100) and the second one is 15% ethanol added feul (E15). The fuel properties were given at Table 4.

Table 2. The properties of the exhaust gas analyzer

Exhaust gas analyzer	Operating range	Accuracy
CO (%)	0-15	0.001
NO (ppm)	0-9999	1 ppm
HC (ppm)	0-5000	1 ppm
O_2 (%)	0-20	0.01
CO_2 (5)	0-25	0.1
Lambda	0.6-4	0.001

Table 3. Technical properties of the cylinder pressure transducer

Model	Kistler 6121 piezo electric
Operating range (bar)	0-250
Measurement precision (pC/bar)	14.7
Operating temperature (ºC)	-50-350
Accuracy (±%)	0.5

Table 4. Fuel Properties

	Ethanol	n-Heptane
Chemical Formula	C2H6O	C7H16
Density (kg/m³)	789	679.5
Octane number	110	0
Lower heating value (MJ/kg)	26.95	44.56
Boiling point (ºC)	78.37	98

Heat release rate was calculated by Equation 1. Thermal efficiency was defined by the ratio between the net work and released energy from fuel (Eq. 2) and the net work was calculated by Equation 3.

$$\frac{dQ}{d\theta} = \frac{k}{k-1} P \frac{dV}{d\theta} + \frac{k}{k-1} V \frac{dP}{d\theta} + \frac{dQ_{heat}}{d\theta} \quad (1)$$

$$\eta_T = \frac{W_{net}}{m_{fuel1} \times Q_{LHV1} + m_{fuel2} \times Q_{LHV2}} \quad (2)$$

$$W_{net} = \int PdV \quad (3)$$

3. Results and Discussion

Figure 2 shows the variation of in-cylinder pressure and heat release rate versus crank angle at 1200 rpm and 60 ºC inlet air temperature. It can be seen that knocking tendency appeared for both fuels at low lambda values. But it was found that ethanol addition had positive effect on knocking owing to its higher octane number when lambda value increased. It can be said that more stable combustion achieved with ethanol addition. What can be clearly seen in Table 4 is ethanol has lower LHV than n-heptane. Lower LHV resulted in a slight increase in HRR. Combustion phasing was retarded and combustion was achieved after top dead center for E15 at almost all lambda values. But lower boiling point of ethanol advance the auto-ignition reactions and decrease the temperature at the end of the compression stroke. However, ethanol has much higher octane number than n-heptane and this provides higher auto-ignition temperatures which led to observe lean mixture zones. This phenomenon can be explained with the higher octane number of ethanol which means higher resistance to auto ignition. Both in-cylinder pressure and heat release rate increased for low lambda values. When the mixture gets richer, charge concentration increases which results in higher reaction rate and accelerated heat release progress that increase maximum pressure.

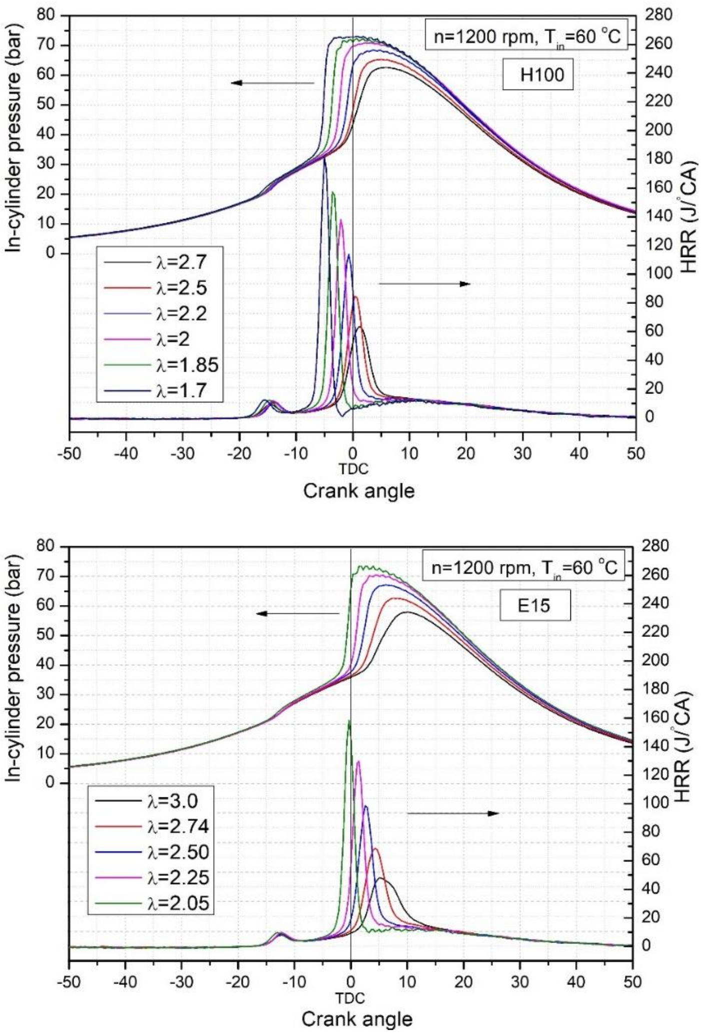

Figure 2. In-cylinder pressure and HRR

The chemical kinetics and pressure-temperature history in the combustion chamber are the main parameters effect the start of combustion in HCCI combustion. Figure 3 shows the variation of CA10 versus lambda. CA10 can be defined as the start of combustion or the crank angle where the 10% mass fraction of the fuel burned. Figure 3 reveals that combustion phasing was retarded with the increase of lambda value. The mixture gets leaner with the increase of lambda value and this means that less fuel molecules contact with oxygen

molecules and combustion starts at later crank angles. Auto ignition was retarted at leaner mixture conditions due to the lower fraction of the fuel. The CA10 values of H100 and E15 were 2.16 (BTDC) and 0.96 (BTDC), respectively, at λ=2.5.

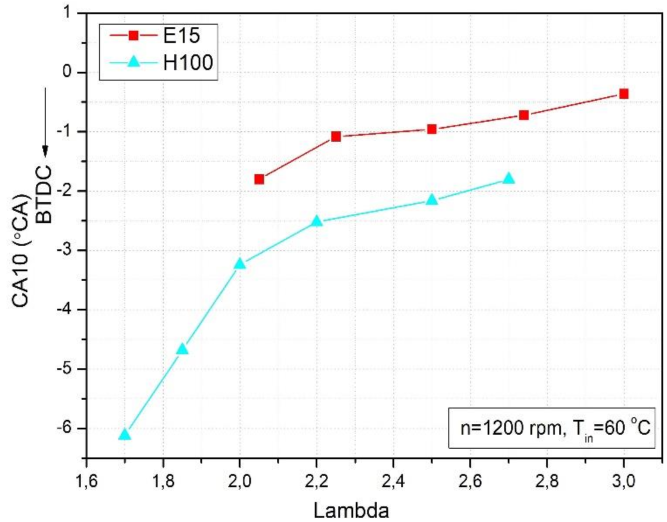

Figure 3. The variation of CA10

Figure 4 represents CA50 and indicated thermal efficiency versus lambda at 1200 rpm and 60 ºC inlet air temperature. Octane number increases with the ethanol addition into the mixture and fuel evaporates more difficulty. For this reason, the burning is prolonged and the start of ignition is delayed. The high reactivity of n-heptane fuel causes HCCI combustion start at earlier cranck angles. Accordingly, the combustion process is developing rapidly and CA50 is advanced. CA50 occurs before the TDC especially in the rich mixture regions due to the high reaction speed in the cylinder and the usage of high reactivity fuel. This causes an increase in the negative work applied on the piston and consequently a low thermal efficiency. As the mixture becomes poor, the reaction rate decreases and the combustion slows down. Accordingly, the CA50 is delayed. The occurrence of CA50 just after the TDC ensures the highest thermal efficiency. The CA50 values of E15 and H100 are 4.32 ºCA (ATDC) and 2.88 ºCA (ATDC) at λ=2.5. The highest efficiencies were obtained at λ=2.5 for E15 and H100 as 48.5% and 47%, respectively.

The variation of ringing intensity was given in Figure 5. Ringing intensity is mostly affected by in-cylinder pressure, pressure rise rate and engine speed. When the Figure 6 was examined that ringing intensity decreases when the lambda increased. The charge mixture gets richer when the lambda decreased and this means the amount of reacting fuel molecules increase which results in higher pressures. The higher density and the oxygen molecule content of ethanol enhance the oxidation reactions and the end of combustion pressure increases rapidly. So, ringing intensity increases. The ringing intensity of E15 and H100 are 8.71 MW/m^2 and 6.09 MW/m^2, respectively, at λ=2.5.

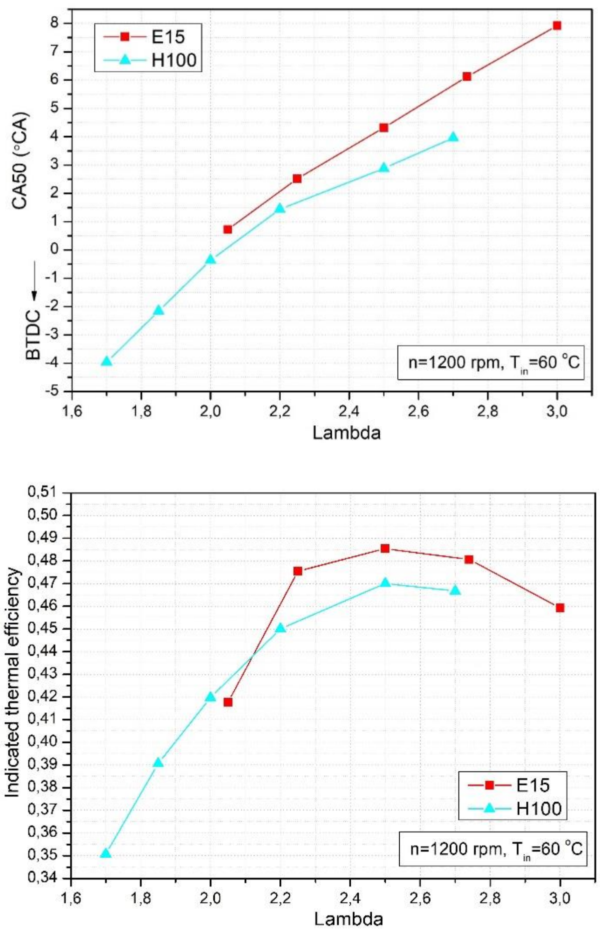

Figure 4. CA50 and indicated thermal efficiency

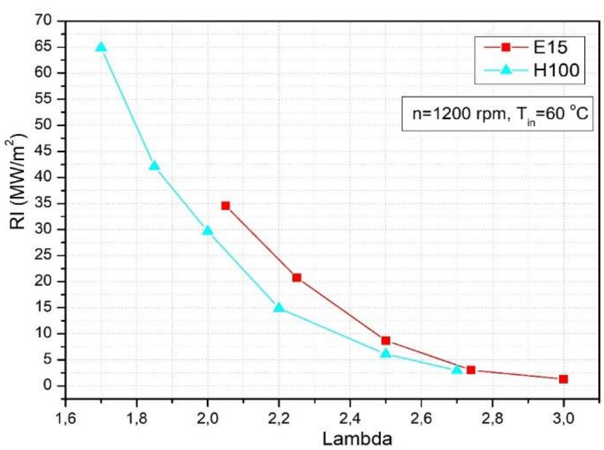

Figure 5. The variation of ringing intensity

Figure 6 shows the variation of HC and CO emissions of the test fuels. Since HCCI combustion occurs at low temperatures, the temperature required for the oxidation of the whole fuel molecules may be insufficient. At the same time, the formation of CO, the incomplete combustion product, is accelerating. When the Figure 6 was mentioned it can be seen that HC emissions decrease with the decrease of lambda. It is because that the excess air increases, sufficient oxygen concentration can be provided for the oxidation of the fuel in the combustion chamber, and so HC decreases. Flame can be extinguished as a result of the inability to ignite the fuel towards rich mixtures, especially in the regions close to the cold cylinder walls. The HC emissions of E15 and H100 were 275 ppm and 348 ppm, respectively, at λ=2.5. The formation of CO increased with the increase of lambda value. As the excess air increases, the gas temperature after combustion decreases and oxidation reactions slow down. This causes to incomplete combustion. The CO emissions of E15 and H100 were 0.1% and 0.08%, respectively, at λ=2.5.

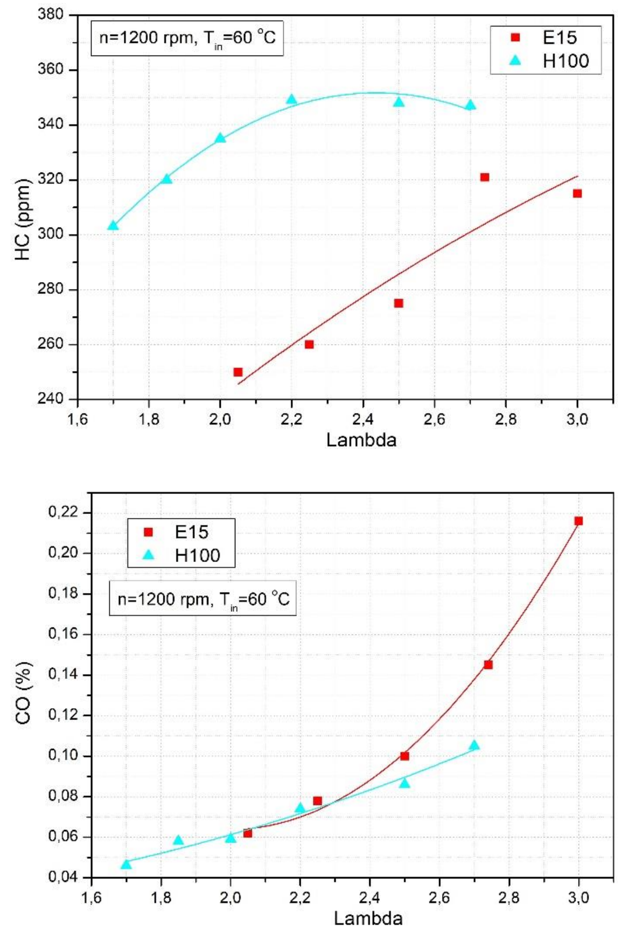

Figure 6. The variation of HC and CO emissions

4. Conclusions

In the current study, the effects of ethanol/n-heptane feul blends in a HCCI engine on the combustion, performance, and exhaust emission characteristics were examined. The experiments were carried out at a constant inlet air temperature of 60 ºC, compression ratio 13 and various lambda values. In-cylinder pressure, heat release rate, CA10, CA50, indicated thermal efficiency, ringing intensity and HC and CO emissions were presented according to the experimental findings. Start of combustion and combustion phase retarded with ethanol addition. CA10 was retarded about 3.12 ºCA at λ=2.5 compared to neat n-heptane. The increasing of lambda value also retarded CA10. CA50 was retarded about 1.5 ºCA with E15 at λ=2.5. Indicated thermal efficiency increased about 3% with ethanol addition at λ=2.5. It is possible to say that ethanol provided more stable combustion in HCCI engine.

Nomenclature

dQ	heat release
dQ_{heat}	heat transferred to cylinder walls
$d\theta$	crank angle
k	ratio of specific heat
P	cylinder pressure (bar)
dV	variation of cylinder volume
W_{net}	net work (joule)
m_{fuel}	consumed fuel per sycle (kg)
Q_{LVH}	lower heating value (kcal)

Conflict of Interest Statement

The author declares that there is no conflict of interest

References

1. Abdelmalek, Z., Alamian, R., Shadloo, M. S., Maleki, A., and Karimipour, A. (2021). Numerical study on the performance of a homogeneous charge compression ignition engine fueled with different blends of biodiesel, Journal of Thermal Analysis and Calorimetry, 143, 2695-2705.
2. Parthasaraty, M., Ramkumar, S., Lalvani, I. J., Elumalai, P.V., Dhinesh, B., Krishnamoorty, R., and Thiyagarajan. (2020). Performance analysis of HCCI engine powered by tamanu methyl ester with various inlet air temperature and exhaust gas recirculation ratios, Fuel, 282, 118833.
3. Alemahdi, N., and Tuner, M. (2020). The effects os 2-ethyl-hexyl nitrate on HCCI combustion properties to compansate ethanol addition to gasoline, Fuel, 270, 117569.
4. Calam, A. (2020) Study on the combustion characteristics of acetone/n-heptane blend and RON50 reference fuels in an HCCI engine at different compression ratios, Fuel, 271, 117646.
5. Solmaz, H. (2020). A comparative study on the usage og fusel oil and reference fuels in an HCCI engine at different compression ratios, Fuel, 273, 117775.
6. Uyumaz, A. (2020). Experimental evaluation of linseed oil biodiesel/diesel fuel blends on combustion, perforamnce and emission characteristics in a DI diesel engine, Fuel, 267, 117150.
7. Çınar, C., Uyumaz, A., Polat, S., Yılmaz, E., Can, Ö., & Solmaz, H. (2016). Combustion and performance characteristics of an HCCI engine utilizing trapped residual gas via reduced valve lift. Applied Thermal Engineering, 100, 586-594.
8. Uyumaz, A. (2015). An experimental investigation into combustion and performance characteristics of an HCCI gasoline engine fueled with n-heptane, isopropanol and n-butanol fuel blends at different inlet air temperatures. Energy Conversion and Management, 98, 199-207.
9. Polat, S., Solmaz, H., Yılmaz, E., Calam, A., Uyumaz, A., & Yücesu, H. S. (2019). Mapping of an HCCI engine using negative valve overlap strategy. Energy Sources, Part A: Recovery, Utilization, and Environmental Effects, 1-15.
10. Solmaz, H. (2015). Combustion, performance and emission characteristics of fusel oil in a spark ignition engine, Fuel Processing Technology, 133, 20-28.
11. Aydoğan, B. (2020). Combustion characteristics, performance and emissions of an acetone/n-heptane fuelled homogenous charge compression ignition (HCCI) engine, Fuel, 275, 117840.
12. Aydoğan, B. (2020). Experimental investigation of tetrahydrofuran combustion in homogenous charge compression ignition (HCCI) engine: Effects of excess air coefficient, engine speed and inlet air temperature, Journal of the Energy Institute, 93, 1163-1176.
13. Calam, A., Solmaz, H., Yılmaz, E., & İçingür, Y. (2019). Investigation of effect of compression ratio on combustion and exhaust emissions in A HCCI engine. Energy, 168, 1208-1216.
14. Çınar, C., Uyumaz, A., Polat, S., Yılmaz, E., Can, Ö., & Solmaz, H. (2016). Combustion and performance characteristics of an HCCI engine utilizing trapped residual gas via reduced valve lift. Applied Thermal Engineering, 100, 586-594.
15. Uyumaz, A. (2015). An experimental investigation into combustion and performance characteristics of an HCCI gasoline engine fueled with n-heptane, isopropanol and n-butanol fuel blends at different inlet air temperatures. Energy Conversion and Management, 98, 199-207.
16. Calam, A. (2020). Effects of the fusel oil usage in HCCI engine on combustion, performance and emission. Fuel, 262, 116503.
17. Calam, A., Aydoğan, B., & Halis, S. (2020). The comparison of combustion, engine performance and emission characteristics of ethanol, methanol, fusel oil, butanol, isopropanol and naphtha with n-heptane blends on HCCI engine. Fuel, 266, 117071.
18. Polat, S., Solmaz, H., Yılmaz, E., Calam, A., Uyumaz, A., & Yücesu, H. S. (2019). Mapping of an HCCI engine using negative valve overlap strategy. Energy Sources, Part A: Recovery, Utilization, and Environmental Effects, 1-15.
19. Uyumaz, A., Aydoğan, B., Calam, A., Aksoy, F., & Yılmaz, E. (2020). The effects of diisopropyl ether on combustion, performance, emissions and operating range in a HCCI engine. Fuel, 265, 116919.
20. Calam, A., Solmaz, H., Yılmaz, E., & İçingür, Y. (2019). Investigation of effect of compression ratio on combustion and exhaust emissions in A HCCI engine. Energy, 168, 1208-1216.
21. Polat, S. (20209. An experimental investigation on combustion, performance and ringing operation characteristics of a low compression ratio early direct injection HCCI engine with ethanol fuel blends, Fuel, 277, 118092, 2020.
22. Gawale, G. R., and Srinivasulu, G. N. (2020). Experimental investigtion of ethanol/diesel and ethanol/biodiesel on dual fuel mode HCCI engine for different engine load conditions, Fuel, 263, 116725.
23. Taghavifar, H., Nemati, A., and Walther, J. H. (2019). Combustion and exergy analysis of multi-component diesel-DME-methanol blends in HCCI engine, Energy, 187, 115951.
24. Gharehghani, A. (2019). Load limits of an HCCI engine fueled with natural gas, ethanoli and methanol, fuel, 239, 1001-1014.
25. Bendu, H., and Sivalingam, M. (2016). Experimental investigation on the effect of charge temperature ethanol fueled HCCI combustion engine, journal of Mechanical Science and Technology, 30(10), 4791-4799.

Engineering Perspective 1 (1): 11-21, 2021

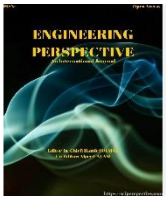

e-ISSN:2757-9077

ENGINEERING PERSPECTIVE

https://sciperspective.com/

Research Paper

Comparison of Energy Consumption of Different Electric Vehicle Power Systems Using Fuzzy Logic-Based Regenerative Braking

Enes Yurdaer[1], Tolga Kocakulak[2*]

[1] *Automotive Engineering Department, Faculty of Technology, Gazi University, Ankara, 06500, Turkey*
[2]*Vocational School of Technical Sciences, Burdur Mehmet Akif Ersoy University, Burdur, 15100, Turkey*

Abstract

One of the disadvantages of electric vehicles that has not yet been overcome is the long battery refueling time. Besides studies to shorten the battery refueling time, increasing the driving range is also a solution to this problem. Different energy saving methods have been tried to increase the driving range. Regenerative braking is one of the best energy-saving methods in electric vehicles. Among several different strategies for regenerative braking, in this study, a fuzzy logic-based regenerative braking strategy is applied to ensure the best regenerative ratio for electric vehicles in any braking case. Moreover, three electric vehicles with different powertrains are modeled in MATLAB/Simulink, and their regenerative braking effectiveness is compared. Inputs of this fuzzy logic controller were determined as the vehicle speed, brake pedal position, and state of charge data; also, three different driving cycles are utilized for simulation. These models are equipped with REMY HVH250-115 electric motor and a battery with a capacity of 80 kWh. As a result, the energy-saving amounts are ordered from the best to the worst as all-wheel drive, front-wheel drive, and rear-wheel drive configurations. Furthermore, the average energy-saving in the all-wheel drive configuration is calculated as 19.11%, in the front-wheel drive configuration is calculated as 9.38%, and in the rear-wheel drive configuration is calculated as 7.93%.

Keywords: Electric Vehicles, Fuzzy Logic, Regenerative Braking, Vehicle Modeling, Powertrain

History
Received: 14.11.2020
Accepted: 23.03.2021

http://dx.doi.org/10.29228/sciperspective.47590

Author Contacts
**Corresponding Author*
enesyurdaer@gmail.com, tkocakulak@mehmetakif.edu.tr
Orcid: 0000-0001-8437-9457, 0000-0002-1269-6370

1. Introduction

Especially in the last half-century, electric vehicles (EVs) have been brought to the agenda again due to the shortage of fossil fuels and environmentalist attitudes, and studies are being conducted on EVs. Thus, in the near history, EVs became a real rival to conventional vehicles for the first time [1,2].

Up to the present, the most significant disadvantages of EVs compared to the conventional vehicles were limited range and long refueling time [3,4]. However, these studies also led to the development of battery technology and enabled more extended range and relatively shorter refueling time. Therefore, it is considered that usage of conventional vehicles with internal combustion engines will be discontinued in the near future.

Some of the advantages of EVs and their electric motors (EMs) are listed as follows [5-8].

•EMs have high efficiencies and torque value.

•BEVs do not require complex drivetrain design.

•EMs are almost maintenance-free.

•EVs run quite silently, are environmentally friendly and easy to operate.

In addition to these advantages, EVs make regenerative braking possible thanks to their EMs.

In conventional vehicles, braking can be operated only by a mechanical braking system. However, one of the best advantage of EMs is that they can also run as a generator, which enabled the regenerative braking operation.

Regenerative braking is a braking method that uses EM to slow down the vehicle in case of braking. While regenerative braking, EM works in the reverse direction, so that acts as a generator and recharge the battery [9]. Regenerative braking provides [10-13], much better control of braking, effectiveness in stop-and-go driving conditions, less frequently maintenance of mechanical braking system and better energy consumption compared to conventional braking.

Under proper circumstances, 8-25% of energy saving can be procured by regenerative braking. Moreover, regenerative braking is considered as the most attractive strategy for energy saving in EVs because it does not require any sizeable extra equipment [14].

Theoretically, a significant proportion of braking operation can be supplied by regenerative braking. However, a suitable proportion of regenerative braking must be supplied in reality due to driving safety aspects. For this reason, different regenerative braking strategies were created [15,16]. There are two common regenerative braking strategies as serial and parallel strategies [17]. In the parallel strategy, regenerative braking and mechanical braking start simultaneously, and regenerative brake operates until peaks. In the serial strategy, regenerative braking starts before mechanical braking, and the mechanical braking starts only when the regenerative brake peaks [18].

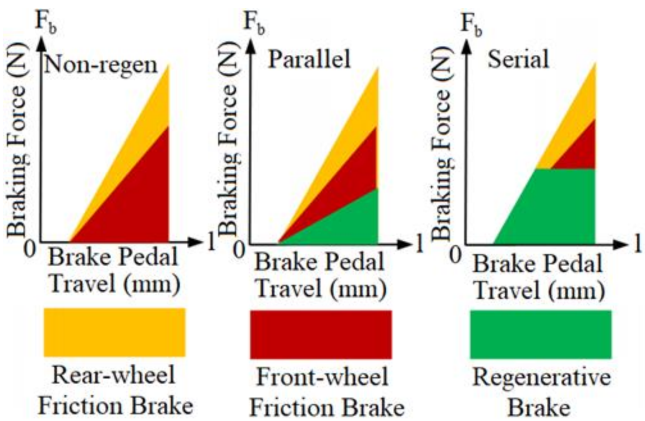

Figure 1. Serial, parallel and non-regen strategies [19]

In the serial strategy, the regenerative braking ratio can be increased compared to the parallel regenerative braking strategy. However, it has a limited part of the total braking in order to avoid problems that might occur in active driving safety systems [20]. This ratio can also be determined by a fuzzy logic controller, which depends on different essential factors such as state of charge (SOC), brake pedal position (BPP), braking force, speed of the vehicle, and temperature of the battery [21,22].

Uses of simple rules and conventional binary logic are insufficient to provide a proper regenerative braking ratio continuously. In contrast, this problem can be overcome by a fuzzy logic controller algorithm because different braking situations can be defined by fuzzy sets and rules [14].

In the regenerative braking strategies, different motor layouts have a considerable effect on energy saving. All-wheel drive (AWD) configurations are quite better than front-wheel drive (FWD) and rear-wheel drive (RWD) configurations in energy-saving comparison because in AWD configurations braking force on both front, and rear axles can be recovered by regenerative braking. Furthermore, FWD configurations are relatively more effective in regenerative braking than RWD configurations because of the location of the vehicle's center of gravity, which is generally close to the front side, and the impact of the inertial force while braking [23,24,25].

Zhang et al. applied a fuzzy logic control to the braking system of a hybrid electric vehicle in order to increase energy saving and regenerative braking efficiency. The energy recovered by regenerative braking was improved by 20% with this fuzzy logic control strategy [26]. Xu et al. created a fuzzy logic-based regenerative braking strategy for EVs to extend their driving range. Braking force, vehicle speed, SOC, and battery temperature data were determined as the inputs of the fuzzy logic controller. According to experiment results, the maximum driving range was improved by 25.7% compared with non-regenerative braking system [27]. Maia et al. presented a fuzzy logic model of regenerative braking in order to avoid the use of EV on-board sensors. As the average of two different test results, 4.04 kWh energy in reality, and 4.83 kWh energy in the simulation were recovered by regenerative braking [28]. Tao et al. proposed a regenerative braking control strategy based on fuzzy logic for an EV with four in-wheel motors. In order to increase energy-saving efficiency and protect the battery, the SOC variable has been taken into account. Under NEDC, energy recovery efficiency was observed as %17.6 [29]. Xiao et al. proposed a new regenerative braking strategy based on a fuzzy logic controller with SOC, motor speed, and brake strength inputs. This strategy was simulated under different driving cycles and a braking scenario, compared to two different braking strategies. According to the results, the braking performance of the model, which has a fuzzy logic-based regenerative braking strategy, was improved by 21.1% for NEDC [30]. Xin et al. created two different composite brake control strategies based on a fuzzy logic controller for load-isolated electric buses and determined SOC and the braking intensity data as the inputs of this fuzzy logic controller. According to simulation results, the driving range of the vehicle was improved by 7.74%, and the energy-saving rate was improved by 11.05% [31].

In the previous study, which is proposed by Kocakulak and Solmaz, three different hybrid vehicle configurations, pre-transmission parallel hybrid, post-transmission parallel hybrid, and serial hybrid, were modeled. Moreover, their average fuel consumption was calculated and compared for different driving cycles. Also, a fuzzy logic-based regenerative braking strategy was created for these models where the inputs of this fuzzy logic controller are SOC, vehicle speed, battery current and pedal position. Under the ECE 15 driving cycle, the energy-saving amounts were ordered from the best to the worst as series (%14.22), pre-transmission parallel (%11.5), and post-transmission parallel hybrid (%9.95) models [22].

In this study, a fuzzy logic-based regenerative braking strategy is created to ensure the ideal regenerative braking ratio in any braking case for three BEVs with different powertrains (FWD, RWD, and AWD). These three BEV configurations are modeled in MATLAB/Simulink.

Specifications of an average four-door sedan are used as simulation parameters. Also, three different driving cycles (NEDC, WLTP Class 3, and FTP-75) are used as reference speed graphs, and the models are controlled by a PID controller. REMY HVH250-115 electric motor is utilized as the EM, and these models are equipped with a battery with a capacity of 80 kWh.

Thus, some values such as driving range, SOC, average energy consumption (AEC), EM torque, EM power, acceleration, speed, and total distance are calculated and commentated. In addition to these data, especially regenerative braking efficiencies of these three configurations are determined and comparatively examined.

2. Material and Method

The BEV models consist of 6 subsystems: driver, EM, driveline, longitudinal resistance forces, battery, and brake.

2.1 Driver Subsystem

Three different drive cycle sources (NEDC, WLTP Class 3, and FTP-75) are utilized as time-dependent reference speed for simulation. The system is controlled by a PID controller, and the vehicle speed is used as feedback data. The output of the PID controller is limited/saturated between -1 and 1. From -1 to 0 is assigned as the BPP, and from 0 to 1 is assigned as the accelerator pedal position (APP). Furthermore, the actual EM torque is obtained by multiplying the APP by the maximum EM torque.

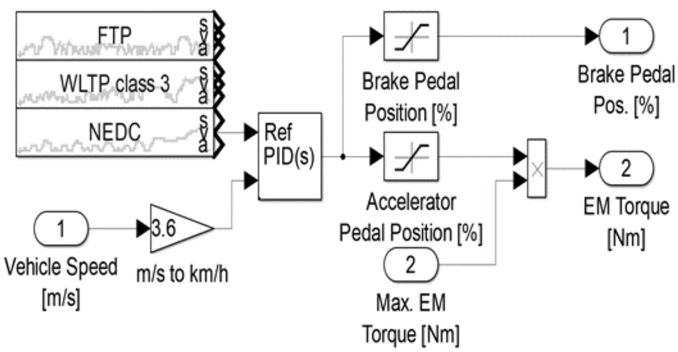

Figure 2. Driver subsystem

2.2 EM Subsystem

It is essential to choose an EM with the proper torque and high-efficiency values for EVs.

In this study, specifications of REMY HVH250-115 Electric Motor are utilized as EM data of the models. The mass of the EM is 57.2 kg, the peak torque is 420 Nm, and the peak efficiency is greater than %95.

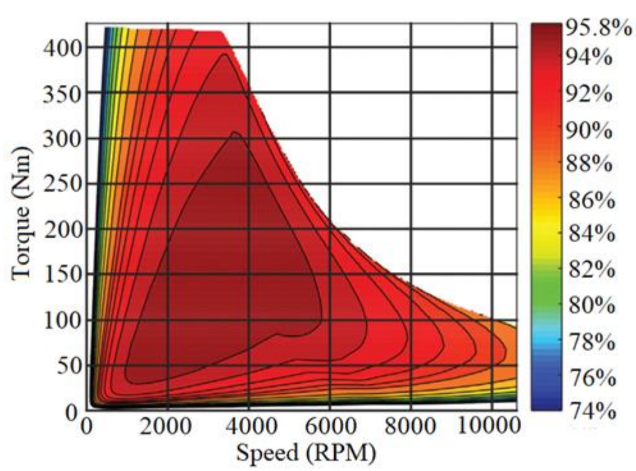

Figure 3. EM Torque Graph [33]

2.3 Driveline Subsystem

Two different equations, to calculate the angular speed of the EM, are obtained for AWD and F/RWD configurations. For F/RWD configurations, the driving force is only transmitted through the front/rear axle.

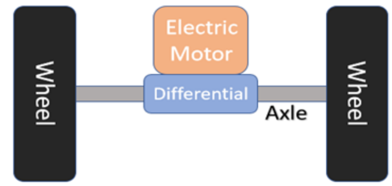

Figure 4. EM layout of F/RWD configurations

For AWD configurations, the driving force is transmitted through both front and rear axles.

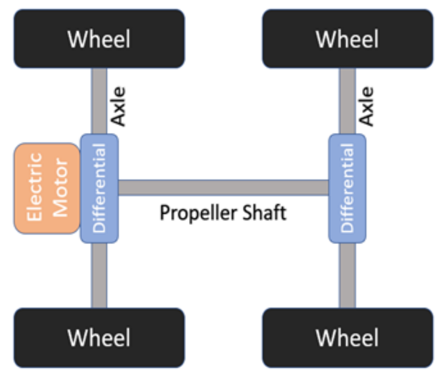

Figure 5. EM layout of AWD configuration

Eq. (1) is used to calculate the angular speed of the EM for F/RWD configurations [9].

$$\omega_{EM} = \int \frac{T_{EM} - \frac{T_w}{i_d \eta_d}}{\frac{J_a + 4J_w}{i_d^2 \eta_d} + J_{EM}} dt \quad (1)$$

Eq. (2) is used to calculate the angular speed of the EM for AWD configurations. AWD power train has double axles. For this reason, an additional axle moment of inertia has been added to the F/RWD vehicle powertrain transfer function.

$$\omega_{EM} = \int \frac{T_{EM} - \frac{T_w}{i_d \eta_d}}{\frac{2J_a + 4J_w}{i_d^2 \eta_d} + J_{EM} + J_s} dt \quad (2)$$

where ω_{EM} EM denotes the angular speed of the EM, T_{EM} denotes the torque of the EM, T_w denotes the torque of the wheel, J_{EM} denotes the mass moment of inertia of the EM, J_w denotes the mass moment of inertia of the wheel, J_a denotes the mass moment of the inertia of the axle, J_s denotes the mass moment of the inertia of the propeller shaft, i_d denotes the final drive reduction ratio, and η_d denotes the efficiency of the final drive.

2.4 Longitudinal Resistance Forces Subsystem

In this study, only longitudinal vehicle dynamics are considered. Neither active safety systems nor lateral/vertical vehicle dynamics are considered.

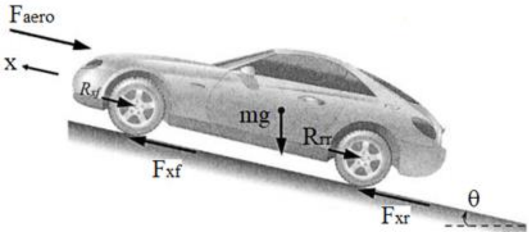

Figure 6. Longitudinal forces acting on the vehicle [34]

The external longitudinal forces acting on the vehicle that moves on an inclined road are aerodynamic drag forces, gravitational forces, longitudinal traction forces on tires, and rolling resistance forces [34].

$$F_i = F_{xf} + F_{xr} - F_{aero} - R_{xf} - R_{xr} - mgsin(\theta) \quad (3)$$

Total traction force (F_{tr}) can be expressed as the sum of the longitudinal traction forces at both front and rear tires.

$$F_{tr} = F_{xf} + F_{xr} \quad (4)$$

Also, the term of '$mgsin(\theta)$' can be described as the gravitational load on the vehicle. Besides all these, aerodynamic drag force, rolling resistance force, and inertial force can be described as in Eq. (6).

$$F_{tr} = ma + \frac{1}{2}\rho C_d A_f (V + V_{wind})^2 + F_z C_{rr} \quad (5)$$

where F_{xf} denotes the longitudinal traction force at the front tires, F_{xr} denotes the longitudinal traction force at the rear tires, F_{aero} denotes the longitudinal aerodynamic drag force, R_{xf} denotes the force due to rolling resistance at the front tires, R_{xr} denotes the force due to rolling resistance at the rear tires, m denotes the mass of the vehicle, a denotes the acceleration of the vehicle, g denotes the gravitational acceleration, θ denotes the angle of inclination, F_i denotes the inertial force of the vehicle, ρ denotes the mass density of air, C_d denotes the aerodynamic drag coefficient, A_f denotes the projected frontal area of the vehicle in the direction of travel, V denotes the longitudinal vehicle velocity, V_{wind} denotes the wind velocity (positive for a headwind and negative for a tailwind), F_z denotes the normal force to the tire, and C_{rr} denotes the rolling resistance coefficient.

2.5 Battery Subsystem

The BEV models are equipped with a battery with a capacity of 80 kWh. The battery power is determined by dividing EM power by EM efficiency in order to obtain total energy consumption of the system (Accessory load is also considered). The obtained energy consumption data are utilized to calculate battery current, AEC, and SOC. Also, the initial value of SOC is determined as 90% to increase regenerative braking efficiency during the simulation.

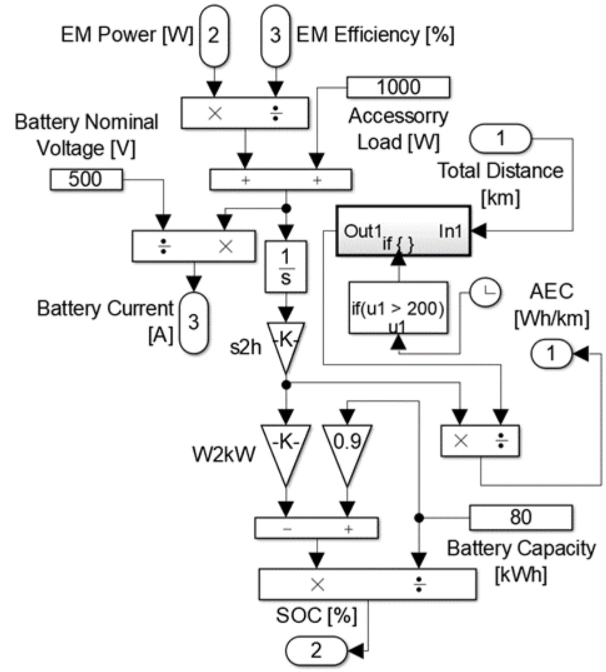

Figure 7. Battery Subsystem

2.6 Brake Subsystem

While the normal force distribution on the tires is being determined, the net pitch torque on the vehicle can be assumed as zero, which means that the pitch angle of the vehicle is assumed to reach a steady-state value [34].

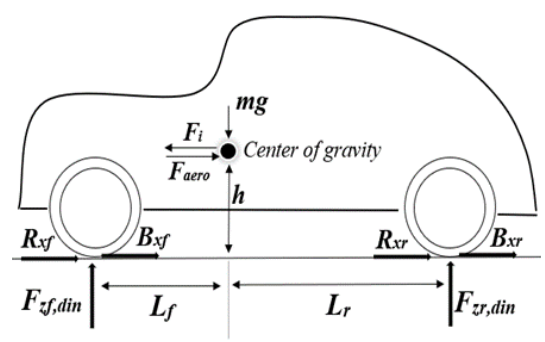

Figure 8. The normal force distribution on tires during braking

$F_{zf,din}$ is described by taking moments about the contact point of the rear tire (Fig. 8).

$$F_{zf,din} = \frac{mgL_r + h(F_i - F_{aero})}{L_f + L_r} \quad (10)$$

$F_{zr,din}$ is described by taking moments about the contact point of the rear tire (Fig. 8).

$$F_{zr,din} = \frac{mgL_f + h(F_{aero} - F_i)}{L_f + L_r} \quad (11)$$

Maximum adhesion between front tires and road while braking is described as in Eq. (12).

$$B_{xf} = \mu F_{zf,din} \tag{12}$$

Maximum adhesion between rear tires and road while braking is described as in Eq. (13).

$$B_{xr} = \mu F_{zr,din} \tag{13}$$

where $F_{zf,din}$ denotes the normal force at the front tires, $F_{zr,din}$ denotes the normal force at the rear tires, B_{xf} denotes the maximum braking force at the front tires, B_{xr} denotes the maximum braking force at the rear tires, L_f denotes the distance between front tires and center of gravity, L_r denotes the distance between rear tires and center of gravity, h denotes the height of the center of gravity, and μ denotes the adhesion coefficient of the wheels.

There are three different regenerative braking strategies for each configuration. For this reason, three different braking subsystems should be set.

In the colored areas, maximum adhesion between front/rear tires and road, which refers to the maximum braking force of the related tire, is calculated. Then, the actual braking force on the related tire is obtained by multiplying the BPP by the maximum braking force (Fig. 9).

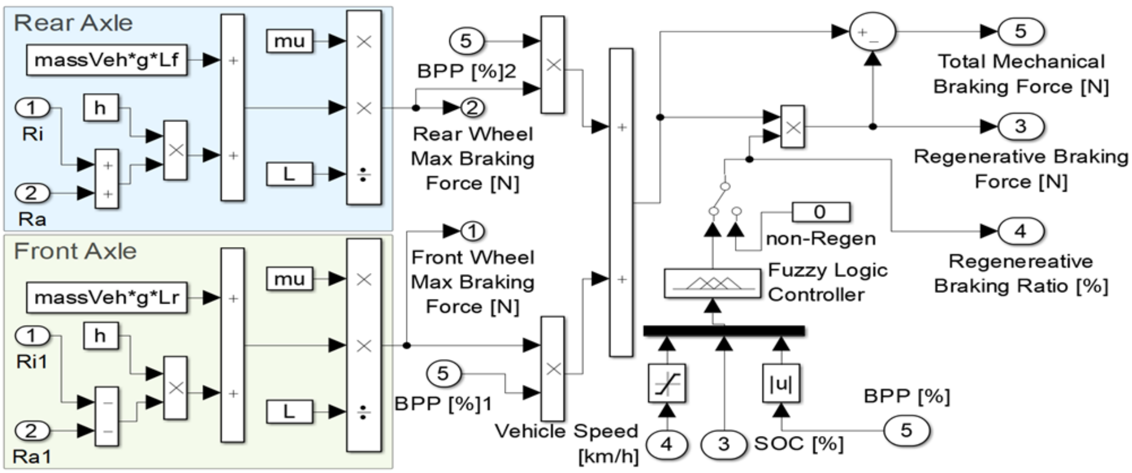

Fig. 9. AWD Brake Subsyste

Regenerative braking is only possible with the braking force on front wheels for FWD configuration and with the braking force on rear wheels for the RWD configuration. However, it is both possible with the braking force on the front and rear wheels for the AWD configuration.

Moreover, the fuzzy logic controller determines the regenerative braking ratio in all cases accurately, and this ratio is utilized to calculate the regenerative braking force.

A Mamdani fuzzy logic controller with three inputs and one output is created to determine the regenerative braking ratio. Input data of the fuzzy logic controller are determined as vehicle speed, SOC, and BPP. Moreover, the output of the fuzzy logic controller is determined as the regenerative braking ratio.

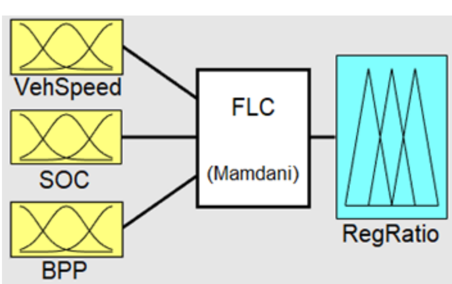

Figure 10. Fuzzy logic controller

For vehicle speed variable, membership functions are determined as low, medium, and high speeds in the range of 0-200 km/h. Vehicle speed has a significant effect on brake safety [14]. If the vehicle speed is low, the regenerative braking ratio should also be low to ensure braking safety. If the vehicle speed is medium, the regenerative braking ratio can be increased correspondingly. The condition, where the vehicle speed is high, is determined as the optimum stage for regenerative braking.

For the SOC variable, membership functions are determined as a low, medium, and high in the range of 0-1. If SOC value is lower than 10%, the inner resistance of the battery has a high value, which is inappropriate for charging. For this reason, the regenerative braking ratio should be low at this stage. If SOC value is between 10% and 90%, it is the ideal situation to charge the battery with a large current, and the regenerative braking ratio should be increased correspondingly. If SOC value is higher than 90%, the regenerative braking ratio should be decreased to prevent the deposit of li-on [14]. For the BPP variable, membership functions are determined as low, medium, and high demands in the range of 0-1.

If braking demand is low, it is the optimum stage for regenerative braking. The EM can ensure most of the braking demand, and it enables high energy saving. If braking demand is high, a quick response should be provided to the system. For this reason, the majority of the braking force is supplied by mechanical braking. Furthermore, the regenerative braking ratio takes the lowest values at this stage. The medium braking demand is inferentially generated between these two stages. For the regenerative braking ratio variable, membership functions are determined as very low (VL), low (L), medium (M), high (H), and very high (VH) demands in the range of 0-1.

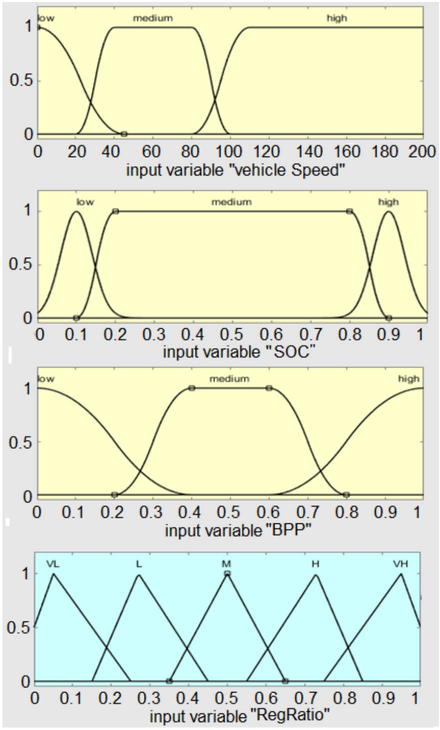

Figure 11. Membership Functions

Table 1. Fuzzy logic rule table

BPP (%)	SOC (%)	Vehicle Speed (km/h)	Regenerative Braking Ratio (%)
High	High	High	L
		Medium	L
		Low	VL
	Medium	High	M
		Medium	L
		Low	VL
	Low	High	L
		Medium	L
		Low	VL
Medium	High	High	M
		Medium	L
		Low	L
	Medium	High	VH
		Medium	H
		Low	H
	Low	High	M
		Medium	M
		Low	L
Low	High	High	M
		Medium	M
		Low	L
	Medium	High	VH
		Medium	VH
		Low	H
	Low	High	H
		Medium	M
		Low	L

A fuzzy logic rule algorithm is created to determine output states corresponding to different values of these three input variables. The rules algorithm is the set of fuzzy rules to be used for inference, and thanks to these if-then rules, the response of the system in different situations can be determined.

In this study, each input variable has three different states, and the fuzzy logic rule table contains 27 if-then rules that include all combinations of these input variables. The fuzzy logic rules are created by considering the conditions of the input variables mentioned above. It also shows that experience is the most significant thing while working with fuzzy logic. The fuzzy logic rule algorithm (if-then rules) and related membership functions are given in Table 1 and Fig. 11, respectively.

2.7 Simulation Parameters

The specifications of the BEV models and the simulation parameters are given in Table 2. Vehicle parameters are taken from studies in the literature, vehicle and product catalogs. The same parameters were used for all vehicle structures examined in the study.

Table 2. BEV models and the simulation parameters

Parameters	Values
Mass of the vehicle	1850 kg
Battery capacity	80 kWh
Battery nominal voltage	500 V
Accessory load	1 kW
Wheel radius (r_w)	0.339 m
The frontal area of the vehicle	2.05 m^2
Aerodynamic drag coefficient (C_d)	0.27
Rolling resistance coefficient (C_{rr})	0.018
Adhesion coefficient (μ)	0.7
Gravitional acceleration (g)	9.81 m/s^2
Air density	1.1839 kg/m^3
Final drive ratio (reduction ratio) (i)	6
Inclination angle	0°
The efficiency of the final drive (η)	0.96
Height of the center of gravity (h)	0.45 m
Distance between rear tires and center of gravity (L_r)	1.5 m
Distance between front tires and center of gravity (L_f)	1.35 m
Mass moment of the wheel	1.15 kgm^2
Mass moment of the propeller shaft	0.55 kgm^2
Mass moment of the axle	0.5 kgm^2
Mass moment of EM	0.086 kgm^2

3. Results and Discussion

3.1 Distance, Speed, and Acceleration Graphs

In the first graph, reference/actual vehicle speed curves and in the second graph, acceleration data of the vehicle are shown (Fig. 12). Total distance, vehicle speed (1st graph), and acceleration (2nd graph) data are obtained from the EM speed data, which is calculated in the Driveline Subsystem. As it is seen in the first graph, reference speed overlaps with the actual vehicle speed, which affirms the truth of the others (Fig 12).

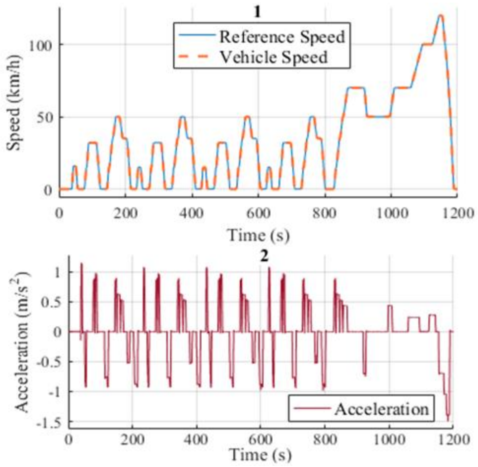

Figure 12. Speed and acceleration graphs (NEDC)

The vehicle reaches to 11 km in NEDC, 23.3 km in WLTP Class 3, and 17.77 km in FTP-75. Moreover, the average speed of the vehicle is 33.6 km/h in NEDC, 46.5 km/h in WLTP Class 3, and 34.1 km/h in FTP-75 (Table 3).

Also, the operating time of NEDC is 1200 seconds, WLTP Class 3 is 1800 seconds, and FTP-75 is 1874 seconds.

Table 3. Specifications of driving cycles

	Total Distance (km)	**Maximum Speed (km/h)**	**Average Speed (km/h)**
NEDC	11	120	33.6
WLTP Class 3	23.3	131.3	46.5
FTP-75	17.77	91.25	34.1

3.2 Distance, Speed, and Acceleration Graphs

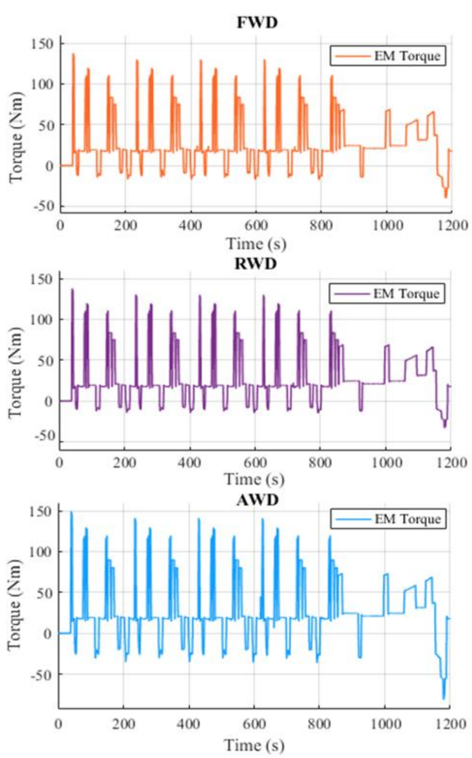

Figure 13. EM Torque graphs (NEDC)

EM torque graphs for FWD, RWD, and AWD models are shown in the first, second, and third lines, respectively (Fig. 13).

EM torque depends on APP and BPP values. When the pedal position is greater than 0, which is driving mode, EM torque takes positive values. When the pedal position is smaller than 0, which is the braking mode, EM torque takes negative values proportional to the regenerative braking ratio. As it is seen in Fig. 13, the driving time is considerably more than the regenerative braking time. EM power and battery current also take negative values during regenerative braking.

Given regenerative braking times, the FWD model has a relatively more regenerative braking time than the RWD model. In contrast, the AWD model has a considerably more regenerative braking time than both.

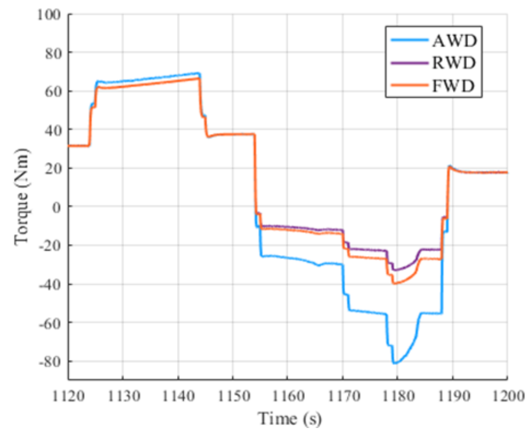

Figure 14. EM Torque comparison (NEDC)

In Fig. 14, EM Torque curves for FWD, RWD, and AWD configurations are given in the same graph. Only the last 80 seconds of the simulation are considered in order to make the graph more understandable. As can be seen from this comparative graph, FWD and RWD configurations have the same values during the driving mode. However, the FWD configuration is more effective than the RWD configuration during regenerative braking. Besides, the AWD configuration sometimes takes different values during the driving mode because of its driveline equation is different from the others. Furthermore, AWD configuration is quite active during regenerative braking compared to the others.

3.3 Regenerative/Mechanical Braking Forces Graphs

Regenerative braking force (RBF) graphs for FWD, RWD, and AWD models are shown in the first, second, and third lines, respectively (Fig. 15).

As it is seen in Fig. 15, the FWD model has a relatively higher RBF than the RWD model. In comparison, the AWD model has a considerably higher RBF than both, which means AWD configuration has a more significant proportion of regenerative braking during braking compared to FWD and RWD configurations.

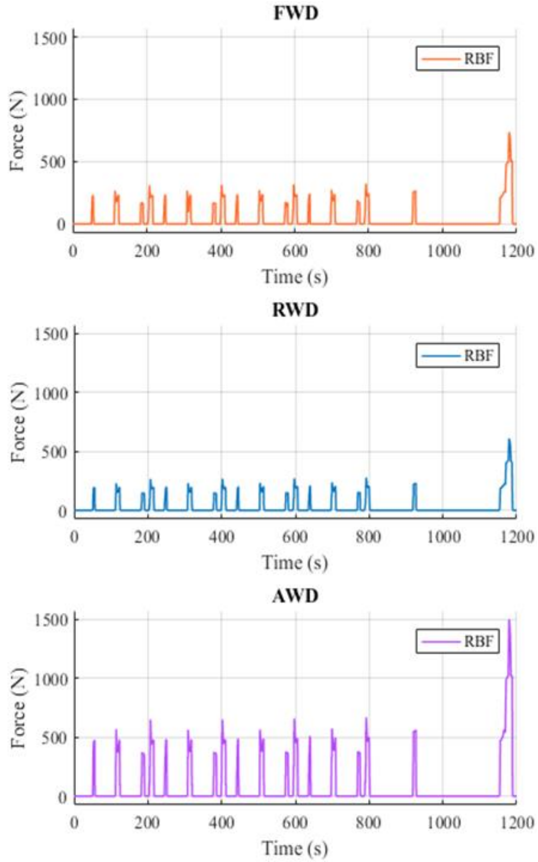

Figure 15. Regenerative Braking Forces graphs (NEDC)

In Fig. 16, RBF curves for FWD, RWD, and AWD configurations are given in the same graph. Only the last one-third of the simulation is considered in order to make the graph more understandable. As can be seen from this comparative graph, the maximum RBF observed during braking for the FWD configuration is approximately 735 N, for the RWD configuration approximately 605 N, and for the AWD configuration approximately 1500 N. Also, average force values during regenerative braking are ordered from the highest to the smallest as AWD, FWD, and RWD models.

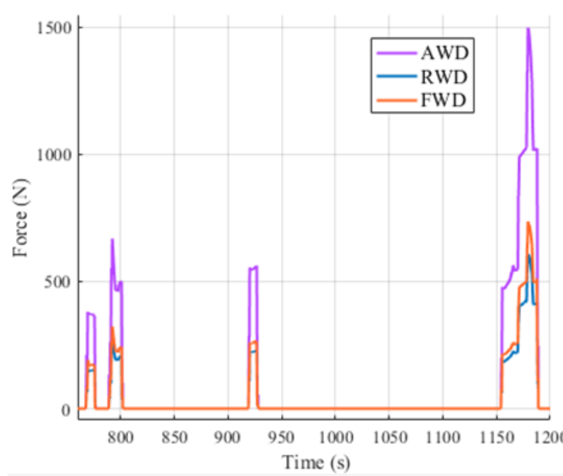

Figure 16. Regenerative Braking Forces comparison (NEDC)

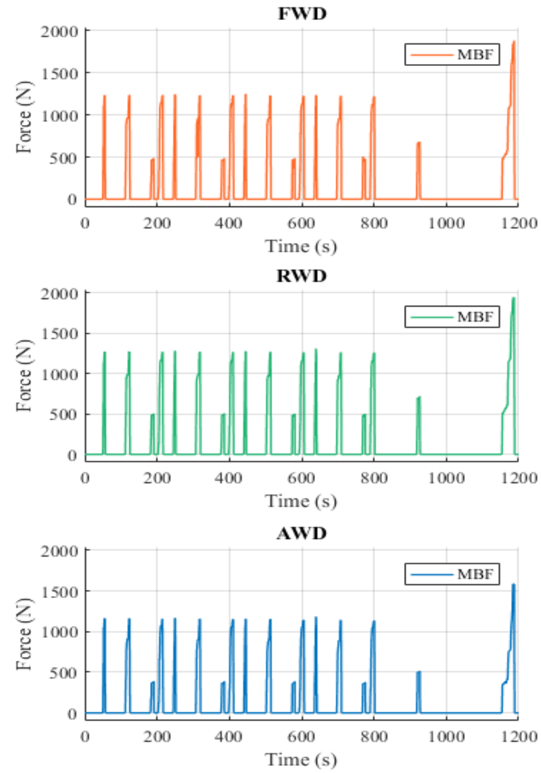

Figure 17. Mechanical Braking Forces graphs (NEDC)

Mechanical braking force (MBF) graphs for FWD, RWD, and AWD models are shown in the first, second, and third lines, respectively (Fig. 17).

As it is seen in Fig. 17, AWD configuration has the smallest proportion of mechanical braking while braking compared to FWD and RWD configurations. Moreover, the RWD model has a higher MBF than both, which means RWD configuration has a more significant proportion of mechanical braking during braking compared to FWD and AWD configurations.

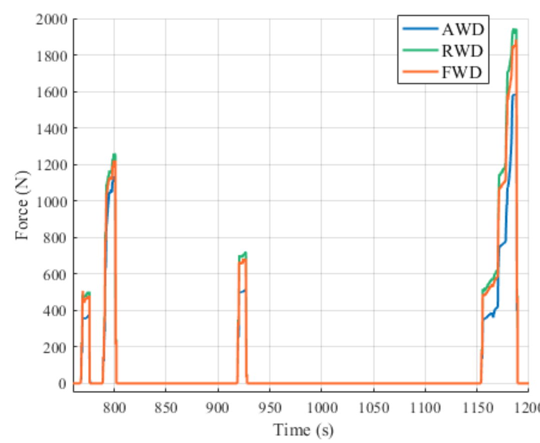

Fig. 18. Mechanical Braking Forces comparison (NEDC)

In Fig. 18, MBF curves for FWD, RWD, and AWD configurations are given in the same graph. Only the last one-third of the simulation is considered in order to make the graph more understandable. As can be seen from this comparative graph, the maximum MBF observed during braking for the FWD configuration is approximately 1850 N, for the RWD configuration 1950 N, and for the

AWD configuration 1600 N. Also, average force values during mechanical braking are ordered from the highest to the smallest as RWD, FWD, and AWD models.

3.4 State of Charge Graphs

In Fig. 19, SOC values of both regenerative and non-regenerative configurations of FWD, RWD, and AWD models are shown. Only the last part of the simulation is considered in order to make the graph more understandable.

As a result of the driving cycles, models with regenerative braking are significantly more economical in terms of energy consumption compared to non-regenerative models.

As it is seen in Fig. 19, the most outstanding energy saving is accomplished in the AWD model. The non-regenerative configurations of the FWD and RWD models have the same results, while the FWD model has slightly better energy consumption characteristics than the RWD model in regenerative braking configurations.

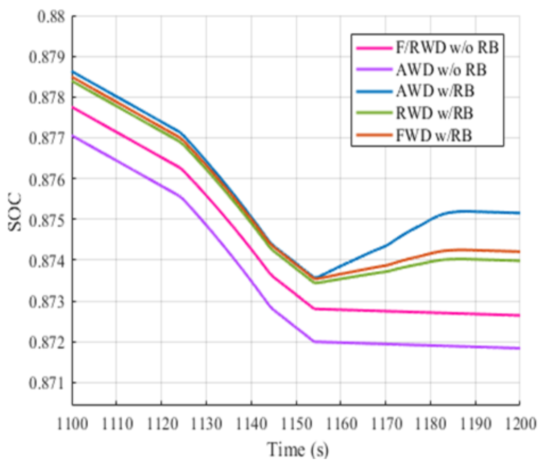

Fig. 19. SOC comparison (NEDC)

3.5 Range and Average Energy Consumption Comparison

Although it is an unhealthy condition for the battery, the system was operated until the SOC value reached 0% from 100% in order to consider the effectiveness of the fuzzy logic-based regenerative braking in any case.

In this period, the distances traveled by the models are determined, and these distances are called as their driving ranges. Also, the AECs of the models are calculated by dividing the battery capacity by the distance traveled.

Table 4. Range and AEC comparison (NEDC)

	w/RB		**w/o RB**	
	Range (km)	**AEC (Wh/km)**	**Range (km)**	**AEC (Wh/km)**
FWD	435.7	183.61	403.08	198.47
RWD	430.8	185.71	403.08	198.47
AWD	463.25	172.69	391.56	204.31

Under NEDC, the AEC of AWD is calculated as 172.69 Wh/km for regenerative configuration and 204.31 Wh/km for non-regenerative configuration. The AEC of FWD is calculated as 183.61 Wh/km for regenerative configuration and 198.47 Wh/km for non-regenerative configuration.

The AEC of RWD is calculated as 185.71 Wh/km for regenerative configuration and 198.47 Wh/km for non-regenerative configuration (Table 4).

Under NEDC, the range of AWD is calculated as 463.25 km for regenerative configuration and 391.56 km for non-regenerative configuration. The range of FWD is calculated as 435.7 km for regenerative configuration and 403.08 km for non-regenerative configuration. The range of RWD is calculated as 430.8 km for regenerative configuration and 403.08 km for non-regenerative configuration (Table 4).

Table 3. Range and AEC comparison (WLTP Class 3)

	w/RB		**w/o RB**	
	Range (km)	**AEC (Wh/km)**	**Range (km)**	**AEC (Wh/km)**
FWD	424.13	188.62	386.56	206.95
RWD	417.92	191.42	386.56	206.95
AWD	458.22	174.59	374.74	213.48

Under WLTP Class 3, the AEC of AWD is calculated as 174.59 Wh/km for regenerative configuration and 213.48 Wh/km for non-regenerative configuration. The AEC of FWD is calculated as 188.62 Wh/km for regenerative configuration and 206.95 Wh/km for non-regenerative configuration. The AEC of RWD is calculated as 191.42 Wh/km for regenerative configuration and 206.95 Wh/km for non-regenerative configuration (Table 5).

Under WLTP Class 3, the range of AWD is calculated as 458.22 km for regenerative configuration and 374.74 km for non-regenerative configuration. The range of FWD is calculated as 424.13 km for regenerative configuration and 386.56 km for non-regenerative configuration. The range of RWD is calculated as 417.92 km for regenerative configuration and 386.56 km for non-regenerative configuration (Table 5).

Table 6. Range and AEC comparison (FTP-75)

	w/RB		**w/o RB**	
	Range (km)	**AEC (Wh/km)**	**Range (km)**	**AEC (Wh/km)**
FWD	440.8	181.49	388.76	205.78
RWD	431.2	185.52	388.76	205.78
AWD	489.67	163.38	373.9	213.96

Under FTP-75, the AEC of AWD is calculated as 163.38 Wh/km for regenerative configuration and 213.96 Wh/km for non-regenerative configuration. The AEC of FWD is calculated as 181.49 Wh/km for regenerative configuration and 205.78 Wh/km for non-regenerative configuration.

The AEC of RWD is calculated as 185.52 Wh/km for regenerative configuration and 205.78 Wh/km for non-regenerative configuration (Table 6).

Under FTP-75, the range of AWD is calculated as 489.67 km for regenerative configuration and 373.9 km for non-regenerative configuration. The range of FWD is calculated as 440.8 km for regenerative configuration and 388.76 km for non-regenerative configuration. The range of RWD is calculated as 431.2 km for regenerative configuration and 388.76 km for non-regenerative configuration (Table 6).

4. Conclusions

In this study, the regenerative braking effectiveness of three different BEVs with different powertrains (FWD, RWD, and AWD) was determined by simulation. Besides, non-regenerative configurations of these systems were utilized for comparison. Various values, such as the driving range, AEC, and SOC, were obtained.

When comparing regenerative configurations with non-regenerative configurations, the energy-saving amounts are ordered from the best to the worst as AWD, FWD, and RWD models.

Under NEDC, 15.48% energy saving in the AWD model, 7.49% in the FWD model, and 6.43% in the RWD model were observed. Thanks to the fuzzy logic-based regenerative braking strategy, 71.69 km extra range in the AWD model, 32.62 km in the FWD model, and 27.72 km in the RWD model were observed.

Under WLTP Class 3, energy saving in the AWD model is 18.22%, in the FWD model is 8.86%, and in the RWD model is 7.5%. Moreover, additional range supplied by regenerative braking is 83.48 km in AWD, 37.57 km in FWD, and 31.36 km in RWD models.

Under FTP-75, energy saving in the AWD model is 23.64%, in the FWD model is 11.8%, and in the RWD model is 9.85%. Moreover, additional range supplied by regenerative braking is 115.77 km in AWD, 52.04 km in FWD, and 42.44 km in RWD models.

The arithmetic mean of the energy-saving values, which is supplied by fuzzy logic-based regenerative braking, in these three driving cycles is calculated.

Consequently, the mean energy-saving in AWD configuration is calculated as 19.11%, in FWD configuration is calculated as 9.38%, and in RWD configuration is calculated as 7.93%.

The reason why the FWD model has higher energy-saving potential than the RWD model is that the braking force on the front axle is greater than the braking force on the rear axle. Therefore, the RBF is higher in the FWD model.

Also, the AWD model naturally has a higher energy-saving potential than the other two models since the braking force on both axles can be used in regenerative braking on the AWD model.

As with any modeling, there are certain assumptions and neglected parameters in this study in order to simplify the models as much as possible, with a small amount of error.

In order to improve this study;

•A more advanced battery subsystem can be created by considering factors such as battery temperature and battery voltage as dependent variables.

•Vertical/lateral vehicle dynamics and active driving safety systems can be considered. Thus, an inclined driving cycle can be created and applied.

•Driving cycles have relatively low acceleration and low braking demands. The effect of the fuzzy logic-based regenerative braking system can be better analyzed by creating an advanced braking scenario.

•The regenerative braking ratio, which is the output of the fuzzy logic controller, can be defined more gradually. Also, the fuzzy rules table can be developed by investigating various braking situations.

•In the FWD, RWD, and AWD configurations, the exact location of the vehicles' center of gravity can be explored.

Nomenclature

NEDC	New European Driving Cycle
WLTP	Worldwide Harmonised Light Vehicles Test Procedure
FTP-75	Federal Test Procedure
BEV	Battery Electric Vehicle
EM	Electric Motor
FWD	Front-Wheel Drive
RWD	Rear-Wheel Drive
AWD	All-Wheel Drive
BPP	Brake Pedal Position
APP	Accelerator Pedal Position
AEC	Average Energy Consumption
SOC	State of Charge
RB	Regenerative Braking
RBF	Regenerative Braking Force
MBF	Mechanical Braking Force
W/	With…
W/O	Without…

Conflict of Interest Statement

The authors declare that there is no conflict of interest.

CRediT Author Statement

Enes Yurdaer: Methodology, Data curation, Writing - review & editing, **Tolga Kocakulak:** Conceptualization, Supervision, Writing - review & editing, Validation

References

1. Ekici, Y. E., & Nusret, T. A. N. (2019). Charge and dis-charge characteristics of different types of batteries on a hybrid electric vehicle model and selection of suitable bat-tery type for electric vehicles. International Journal of Automotive Science and Technology, 3(4), 62-70. https://doi.org/10.30939/ijastech..527971
2. Kunt, M. A. (2020). Advisor Based Modelling of Regen-erative Braking Performance of Electric Vehicles at Dif-ferent Road Slopes. International Journal of Automotive Science and Technology, 4(2), 98-104. https://doi.org/10.30939/ijastech..717097
3. Un-Noor, F., Padmanaban, S., Mihet-Popa, L., Mollah, M.N., Hossain, E. (2017). A Comprehensive Study of Key Electric Vehicle (EV) Components, Technologies, Challenges, Impacts, and Future Direction of Develop-ment. Energies , 10, 1217. https://doi.org/10.3390/en10081217
4. Kıyaklı, A. O., & Solmaz, H. (2018). Modeling of an Electric Vehicle with MATLAB/Simulink. International Journal of Automotive Science And Technology, 2(4), 9-15. https://doi.org/10.30939/ijastech..475477
5. D. U. Thakar and R. A. Patel (2019). Comparison of Advance and Conventional Motors for Electric Vehicle Application, 2019 3rd International Conference on Recent Developments in Control, Automation & Power Engi-neering (RDCAPE), NOIDA, India, pp. 137-142, doi: 10.1109/RDCAPE47089.2019.8979092.
6. J. Ruan and Q. Song (2019). A Novel Dual-Motor Two-Speed Direct Drive Battery Electric Vehicle Drivetrain, in IEEE Access, vol. 7, pp. 54330-54342, doi: 10.1109/ACCESS.2019.2912994.
7. C. A. Bilatiu, S. I . Cosman, R. A. Martis, C. S. Martis and S. Morariu,

(2019). Identification and Evaluation of Electric and Hybrid Vehicles Propulsion Systems. 2019 Electric Vehicles International Conference (EV). doi:10.1109/ev.2019.8892965

8. Ghasri, M., Ardeshiri, A., & Rashidi, T. (2019). Per-ceived Advantage in Perspective Application of Integrat-ed Choice and Latent Variable Model to Capture Electric Vehicles Perceived Advantage from Con-sumers Perspec-tive. arXiv preprint arXiv:1905.11606.
9. Kocakulak, T., & Solmaz, H. (2020). HCCI Menzil Art-tirici Motor Kullanilan Seri Hibrit Bir Aracin Modellen-mesi. Gazi Üniversitesi Fen Bilimleri Dergisi Part C: Tasarım Ve Teknoloji, 8(2), 279-292. https://doi.org/10.29109/gujsc.670564
10. M. K. Yoong, Y. H. Gan, G. D. Gan, & K.W Chew. (2010). "Studies of regenerative braking in electric vehi-cle," 2010 IEEE Conference on Sustainable Utilization and Development in Engineering and Technol-ogy, Petal-ing Jaya, pp. 40-45, doi: 10.1109/STUDENT.2010.5686984.
11. Heydari, S., Fajri, P., Rasheduzzaman, M., & Sabzehgar, R. (2019). Maximizing regenerative braking energy re-covery of electric vehicles through dynamic low-speed cutoff point detection. IEEE Transactions on Transpor-tation Electrification, 5(1), 262-270.
12. Heydari, S., Fajri, P., Sabzehgar, R., & Rasouli, M. (2019). A Novel Approach for Maximizing Regenerative Braking Energy Extraction of Electric Vehicles Using Motor Performance Lookup Table. In 2019 IEEE Trans-portation Electrification Conference and Expo (ITEC) (pp. 1-5). IEEE. DOI: 10.1109/ITEC.2019.8790633
13. Heydari, S., Fajri, P., Sabzehgar, R., & Asrari, A. (2020). Optimal Brake Allocation in Electric Vehicles for Maxim-izing Energy Harvest-ing During Braking. IEEE Transac-tions on Energy Conversion. DOI: 10.1109/TEC.2020.2994520
14. J. Paterson and M. Ramsay (1993). "Electric vehicle braking by fuzzy logic control," Conference Record of the 1993 IEEE Industry Applica-tions Conference Twen-ty-Eighth IAS Annual Meeting, Toronto, On-tario, Cana-da, pp. 2200-2204 vol.3, doi: 10.1109/IAS.1993.299173.
15. Liu, H., Lei, Y., Fu, Y., & Li, X. (2020). An Optimal Slip Ratio-Based Revised Regenerative Braking Control Strategy of Range-Extended Electric Vehi-cle. Energies, 13(6), 1526. https://doi.org/10.3390/en13061526
16. Zhao, W., Wu, G., Wang, C., Yu, L., & Li, Y. (2019). Energy transfer and utilization efficiency of regenerative braking with hybrid energy storage system. Journal of Power Sources, 427, 174-183. https://doi.org/10.1016/j.jpowsour.2019.04.083
17. Totev, V., Gueorgiev, V., & Rizov, P. (2019). Regenera-tive braking of electric vehicles. In 2019 11th Electrical Engineering Faculty Con-ference (BulEF) (pp. 1-5). IEEE.
18. Zhao, X., Li, L., Wang, X., Mei, M., Liu, C., & Song, J. (2019). Braking force decoupling control without pres-sure sensor for a novel series re-generative brake sys-tem. Proceedings of the Institution of Mechanical Engi-neers, Part D: Journal of Automobile Engineer-ing, 233(7), 1750-1766. https://doi.org/10.1177%2F0954407018785740
19. C. Qiu, G. Wang, M. Meng, and Y. Shen (2018). A nov-el control strat-egy of regenerative braking system for electric vehicles under safety critical driving situations, Energy 149, 329 – 340. https://doi.org/10.1016/j.energy.2018.02.046
20. S. Oleksowicz, K. Burnham, and A. Gajek (2012). On the legal, safety and control aspects of regenerative brak-ing in hybrid/electric vehicles.
21. Martellucci, L., & Giannini, M. (2020). Regenerative Braking Experi-mental Tests and Results for Formula Student Car. Journal of Trans-portation Technologies, 11(1), 78-89. https://doi.org/10.4236/jtts.2021.111005
22. Subramaniyam, K. V., & Subramanian, S. C. (2021). Impact of regen-erative braking torque blend-out characteristics on electrified heavy road vehicle braking performance. Vehicle System Dynamics, 59(2), 269-294. https://doi.org/10.1080/00423114.2019.1677921
23. De Pinto, S., Camocardi, P., Chatzikomis, C., Sorniotti, A., Bottiglione, F., Mantriota, G., & Perlo, P. (2020). On the comparison of 2-and 4-wheel-drive electric vehicle layouts with central motors and single-and 2-speed transmission systems. Energies, 13(13), 3328. https://doi.org/10.3390/en13133328
24. Ju, F., Zhuang, W., Wang, L., & Zhang, Z. (2020). Comparison of four-wheel-drive hybrid powertrain configurations. Energy, 118286. Ju, F., Zhuang, W., Wang, L., & Zhang, Z. (2020). Comparison of four-wheel-drive hybrid powertrain configurations. Energy, 118286. https://doi.org/10.1016/j.energy.2020.118286
25. Tan, F., & Yan, E. (2020). An Efficiency-Based Hybrid Mode Selec-tion Model for A P134 Plug-In Hybrid Powertrain Architecture (No. 2020-01-5001). SAE Technical Paper. https://doi.org/10.4271/2020-01-5001
26. J. Zhang, B. Song, S. Cui and D. Ren (2009). "Fuzzy Logic Approach to Regenerative Braking System," 2009 International Conference on Intelligent Human-Machine Systems and Cybernetics, Hangzhou, Zhejiang, pp. 451-454, doi: 10.1109/IHMSC.2009.120.
27. X. Guoqing, L. Weimin, X. Kun & Song, Zhibin. (2011). An Intelligent Regenerative Braking Strategy for Electric Vehicles. Energies. 4. 1461-1477. 10.3390/en4091461.
28. Maia R., Silva M., Araùjo R., Nunes U. (2015). Electri-cal vehicle modeling : a Fuzzy logic model for regenerative braking. Expert Sys-tems with Applications. Volume 42, Issue 22. https://doi.org/10.1016/j.eswa.2015.07.006
29. Y. Tao, X. Xie, H. Zhao, W. Xu and H. Chen (2017). A regenerative braking system for electric vehicle with four in-wheel motors based on fuzzy control. 2017 36th Chi-nese Control Conference (CCC), Dalian, pp. 4288-4293, doi: 10.23919/ChiCC.2017.8028032.
30. Xiao, Boyi & Lu, Huazhong & Wang, Hailin & Ruan, Jiageng & Zhang, Nong. (2017). Enhanced Regenerative Braking Strategies for Electric Vehicles: Dynamic Per-formance and Potential Analysis. Energies. 10. 1875. 10.3390/en10111875.
31. Xin, Yafei & Zhang, Tiezhu & Zhang, Hongxin & Zhao, Qinghai & Zheng, Jian & Wang, Congcong. (2019). Fuzzy Logic Optimization of Composite Brake Control Strategy for Load-Isolated Electric Bus. Mathematical Problems in Engineering. 2019. 1-14. 10.1155/2019/9735368.
32. Kocakulak, T., & Solmaz, H. (2020). Control of pre and post transmis-sion parallel hybrid vehicles with fuzzy log-ic method and comparison with other power sys-tems. Journal of the Faculty of Engineering and Architec-ture of Gazi University, 35(4), 2269-2286. DOI:10.17341/gazimmfd.709101
33. HVH 250-115 Electric Motor datasheet. https://cdn.borgwarner.com/docs/default-source/default-document-li-brary/remy-pds---hvh250-115-sheet-euro-pr-3-16.pdf?sfvrsn=ad42cd3c_11, last access date: 13.08.2020
34. R. Rajamani (2011). Vehicle dynamics and control, Mechanical Engi-neering Series, Springer US.

Engineering Perspective 1 (1): 22-29, 2021

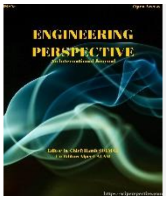

e-ISSN:2757-9077

ENGINEERING PERSPECTIVE

https://sciperspective.com/

Research Paper

Analysis of the Behavior of a Cross-Type Hydraulic Outrigger and Stabilizer Operating Under Determined Loads

Mustafa Karaman[1,2*], Emre Öztürk[3]

[1] *Hidroan Ankara Hidrolik Mak. San. Tic. Ltd. Şti, Ankara, 06374, Turkey*
[2] *Manufacturing Engineering, Graduate School of Natural and Applied Sciences, Gazi University, Ankara, 06500, Turkey*
[3] *Mechanical Engineering, Graduate School of Natural and Applied Sciences, Gazi University, Ankara, 06500, Turkey*

Abstract

In this study, behavior of a fully opened cross type hydraulic outrigger and stabilizer of an aerial ladder firefighting device which is on determined static load is analyzed. This hydraulic outriggers and stabilizer are designed via SOLIDWORKS 2017 software and then analyzing process is run at SIEMENS NX 11.0 NASTRAN software. The location of the center of gravity of the firefighting device and its mass at several use cases is used as input for analysis. Standard equipment's which can work with harmony are chosen for model, since design of a commercially producible model is aimed. Stress, strain values and forces acting on mills are obtained by analysis and then interpreted. When displacement of mass against gravity is -13 mm, displacement of outrigger and stabilizers system is ±4. The maximum stress at system is obtained as 190 MPa when singular values are filtered. Factor of safety is determined as 1,9 for this system. The system is decided as durable according to this study.

Keywords: Analyze, Crane, Firetruck, Hydraulic outriggers, Stabilizers

History
Received: 06.02.2021
Accepted: 20.03.2021

http://dx.doi.org/10.29228/sciperspective.49248

Author Contacts
**Corresponding Author*
mkaraman@hidroan.com.tr, emreozturk0640@gmail.com
Orcid: 0000-0001-9574-9732, 0000-0002-5971-0520

1. Introduction

Structures such as cranes, lifting platforms, aerial ladder firefighting vehicles, and launching platforms, which serve different purposes, were shipped to the area where they would be used and made ready for use after they were assembled at the place of operation in traditional methods. In line with the requirements, these structures were transformed into mobile by mounting on trucks, and as a result, it has been provided to meet the needs more quickly [1, 2]. This situation has led to the need to stabilize and support these mobile vehicles in the different ground and environmental conditions [3, 4]. In line with this need, different stabilizers and outriggers have been developed for different vehicle superstructures. In such vehicles, to ensure the safety of the system and to ensure error-free operation continuity, the reaction forces generated in the stabilizer and outriggers should not increase to very high levels [5-7]. Stabilization of these vehicles is essential to ensure that people around, especially the operator using the vehicle, the material carried, and the vehicle itself work safely, correctly, and without any damage [8,9]. In addition to these parameters, stabilizers and outriggers are of critical importance in terms of the vehicle's ability to operate without harming the personnel and people around during its duty and not to prevent them [10-13].

In the literature, two essential criteria have been used for stabilizers and outriggers: Proper and improper use. Proper use is defined as a situation where the stabilizer and outriggers are fully extended (opened) on firm ground, and improper use is defined as use when the ground is not firm. For the stabilizer and outriggers to perform their tasks effectively, they should be operated on firm ground as much as possible, and equipment that will increase the surface area of the pad should be used in case of operation under soft ground conditions [14]. If the vehicles are not stabilized, serious problems such as rollover (tipping) can occur. Such possible problems that may arise pose a danger at a level that can lead to severe material damage and life threat for the aforementioned mobile platforms and the elements around [15-18]. A study published in 2017 determined that 72% of the crane accidents that occurred worldwide were experienced in mobile cranes. The same study determined that 45% of the accidents in mobile cranes were caused by stabilizer and outriggers, ground subsidence, and overloading [19]. In another study on mobile cranes published in 2017, it was stated that 31% of the accidents experienced in mobile cranes were caused by reasons such as lifting and lowering the load, unbalanced load distribution, load drop, and load acceleration. It has been revealed that 11% of the accidents are caused by reasons related to balancing the load, such as the failure of stabilizer and outriggers, overloading, and loss of control of the center of gravity [20]. In an older study, it was shown that more than 50% of crane accidents occurred due to improper use of the crane or stabilizer and outriggers [21]. As can be seen, in accidents that occur in superstructures worldwide, the rate of stabilizers and outriggers to cause accidents is considerably high. The dangers of such accidents, extending to death, are too severe to ignore. It is seen that stabilizers and outriggers play a significant role in these accidents.

Apart from mobile cranes, there is a need for stabilizing and supporting aerial ladder firefighting vehicles, mobile cargo lifts, and military vehicles such as launching platforms, whose operating logic is similar to mobile cranes and vehicles used in many other different areas. In this study, cross-type stabilizers and outriggers used in aerial ladder firefighting vehicles are analyzed.

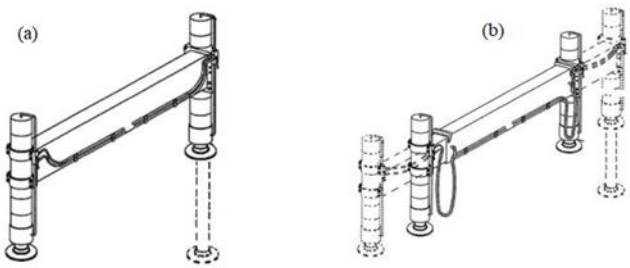

Figure 1. Frequently used stabilizer and outrigger systems

Two of the most frequently used hydraulic stabilizer and outriggers in mobile vehicles are shown in Figure 1. The stabilizing process is carried out by ensuring that the appropriate stabilizer and outrigger types, which have many more types according to the vehicle characteristics and the working area's condition, are mounted on the vehicles. Manufacturing companies use different names in identifying these stabilizer and outrigger types. In the stabilizer and outrigger type shown in Figure 1. (a), the pad parts of the hydraulic stabilizer and outriggers go down directly and become ready for use. This type is called fixed stabilizer and outrigger in the literature. In the stabilizer and outrigger type shown in Figure 1. (b), the stabilizer and outriggers are opened to the right and left before the hydraulic pads touch the ground. This type is called the (side) extending stabilizer and outrigger. According to the operating conditions, the usages in which the right and left stabilizer and outriggers are opened at different rates are also common.

Fixed type hydraulic stabilizer and outriggers are generally preferred in situations where there is a fixed and not long structure on it and does not require the superstructure to extend and rotate. This stabilizer and outrigger structure's task is to transfer the loads generated during the operation of the superstructure to the ground instead of the vehicle chassis.

In (side) extending type stabilizer and outrigger structures, in addition to the features of the fixed type, the stabilizer and outriggers can open and extend at the same rate to the right and left, or they can open and extend separately to the right or only to the left. The extending type stabilizer and outrigger structure allow rotating mechanisms, such as telescopic ladders or cranes, that change their position according to the center of gravity to operate safely without rollover. Figure 2 shows the (side) extending type outriggers in a telescopic ladder fire fighting vehicle. The most important disadvantage of this type of outriggers is that a vast area is needed to open the outriggers to the side.

Figure 2. Hydraulic stabilizer and outriggers on aerial ladder firefighting vehicle

Instead of these stabilizer and outrigger types, cross-type stabilizer and outrigger structures are frequently used in mobile vehicles. In cross-type outriggers, height differences up to 700 mm on the ground surface where the vehicle will operate can be damped thanks to the outriggers' geometric features. The most crucial feature of cross-type outrigger structures is that they can be opened to support the superstructure even in narrow spaces. In narrow streets where firefighting vehicles need to perform tasks frequently, the superstructure can be supported by extending the outriggers under the parked vehicles on the right and left sides. Another feature of the cross-type outriggers that provides an advantage over other outrigger types is that they do not prevent people and personnel from passing over them when the outriggers are open. This feature allows the personnel on duty or other people around to move quickly in emergencies.

In this study, a cross-type stabilizer and outrigger design has been made for an aerial ladder firefighting vehicle. Prior to the design, the center of gravity position and weight values were calculated for the vehicle to be used in different scenarios. Among these calculated values, scenario values that will force the outrigger structure at the maximum level were selected and used as analysis input. Static analysis of the outriggers under the determined system load has been made, and their usability has been evaluated within the firefighting vehicle whose prototype will be produced.

2. Material and Method

2.1 Determining System Components

The stabilizer and outrigger system consists of four separate outriggers, and these outriggers are mounted to each other in pairs, front, and back. The outriggers were designed in a concept that can be mounted on a two-axle class E truck. Each outrigger is driven by two separate hydraulic cylinders, one for side opening and one for ground contact, and the system assembly includes eight hydraulic cylinders in total. While designing the outriggers, considering the prototype production, standard and available materials were used as hydraulic cylinder elements, profiles, and fasteners.

Figure 3 shows the sectional view and perspective view of cylinders and profiles in an outrigger's closed and open position. The basic materials used in the construction can be listed as hydraulic cylinders, hydraulic pistons, hydraulic rods, hydraulic sealing elements, steel sheets, steel box sections, steel shafts, bronze bearings, and hydraulic valves. When the outriggers are fully open, the outriggers reach an overall size of 5475 mm, while the pads have an out-to-out distance of 5400 mm to each other. In this case, the angle of the profiles to the ground is 12˚.

Figure 3. Closed and open position solid model of cross-type outriggers

Using hydraulic load holding (over-center) valves in the pads' cylinders aims to ensure that the system can remain stabilized in case of a sudden pressure change. Using the load measurement sensor in the pads, the load on each outrigger will be measured, and the center of gravity will be kept in the safe zone electronically with this data; thus, controlling the stabilization system will be provided by electronic software.

2.2 Determination of Operating Conditions

While analyzing the structure that will serve as the stabilizer and outrigger of the ladder and rotary table mechanism of an aerial ladder firefighting vehicle, which weighs 18,000 kg with front and rear outrigger groups, the "fully open" position, which is the maximum load-bearing configuration for the outriggers, was used.

2.3 Geometries Used and Geometric Simplification

Components such as hydraulic installation, bolts, circlip, etc., are not included in the simulation model since they do not affect structural integrity. No special modeling has been performed for weld lines (for welds on the part), and continuous geometries represent the bodies. In the model created, sheet metal and profile components are represented by 2D (surface), and 3D geometries represent all other components.

2.4 Numerical Modeling

In the simulation model created for static solutions, profile and sheet metal components (2D geometries) were analyzed with CQUAD8 (8-node, parabolic, -node, parabolic, 2D NASTRAN numerical modeling element), all other 3D components were solved with CTETRA10 (10-node, tetrahedral, parabolic, 3D NASTRAN numerical modeling element) and CHEXA20 elements (20-node, hexahedral, parabolic, 3D NASTRAN numerical modeling element).

The maximum total mass of the vehicle chassis, turntable and ladder components (18 tons) is represented by the 0B CONM2 element (0B NASTRAN numerical modeling element). This element has been placed in accordance with the 45˚ angular position of the turntable as its dimensions are defined in figure 4. The point mass element is connected to the front and rear outrigger assemblies using 1B RBE2 element (1B NASTRAN numerical modeling element (rigid)), assuming that the chassis is enduring (durable). The joints' shafts are modeled with the same diameter 1B CBEAM (1B NASTRAN numerical modeling element (flexible)) numerical modeling elements. The model has a total of 200,844 elements and 732,461 nodes [22].

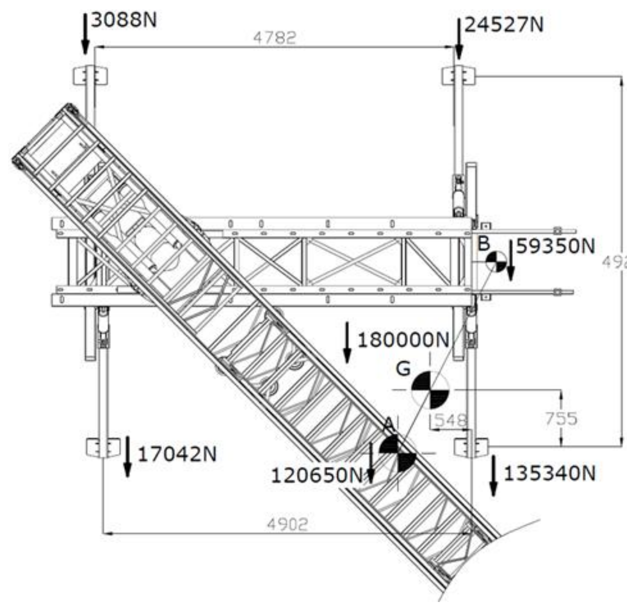

Figure 4. Firefighting vehicle center of gravity position and forces acting on outriggers

In Figure 4, the outriggers' loads can be seen in the scenario created considering the situation where the highest load affects the outriggers. In this state, the analysis was carried out according to the worst case in the load acting on the outriggers, when the firefighting vehicle ladder is synchronous 24 m open and at an angle of 45˚. In Figure 4, point A indicates the center of gravity of the superstructure, point B indicates the center of gravity of the vehicle chassis, while point G indicates the resultant center of gravity. Based on the simulation model created, a static solution was realized in the single scenario (NASTRAN solution sequence: 101). This scenario, which was chosen as the "most challenging loading condition", was prepared using the maximum load elements that the outriggers can carry, and the turntable is positioned at an angle of 45˚ relative to the vehicle chassis. Figure 5 shows the meshed view of the system and outrigger.

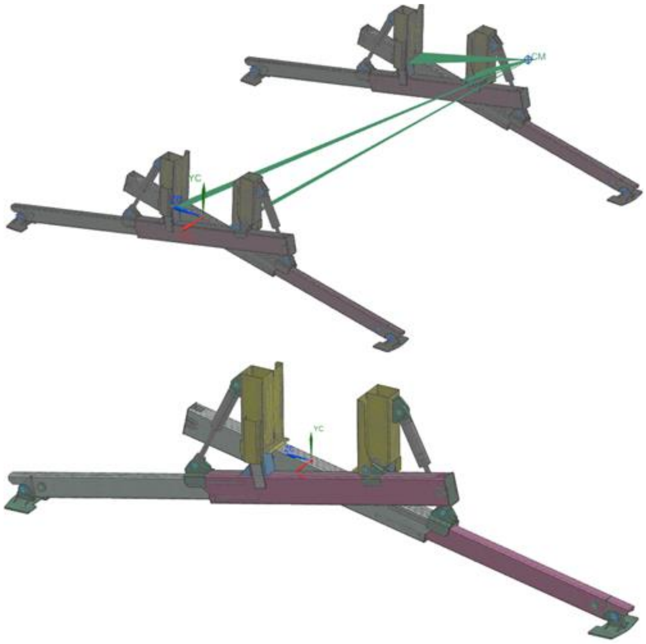

Figure 5. Numerical model of the system and outrigger assembly

2.5 Connections

Besides bolted and welded connection methods, bronze bearings for contact surfaces in friction bearings and shafts in swivel joints are used in the system. In the simulation model created for static solutions, bearing plates and counterparts contact interface connections are modeled with SSC (NASTRAN surface-to-surface contact), and all welded connections are modeled with SSG (NASTRAN surface-to-surface gluing) formulation [22].

2.6 Limiting Conditions

In the stabilizer and outriggers, since it is aimed to transfer the weight of the superstructure to the ground by the contact of the pads with the ground, in the simulation model created for static solutions, the freedom of these regions is restricted by applying "Fixed Constraint" on the base surfaces of the pads. In Figure 6, regions with restricted freedom are shown in orange.

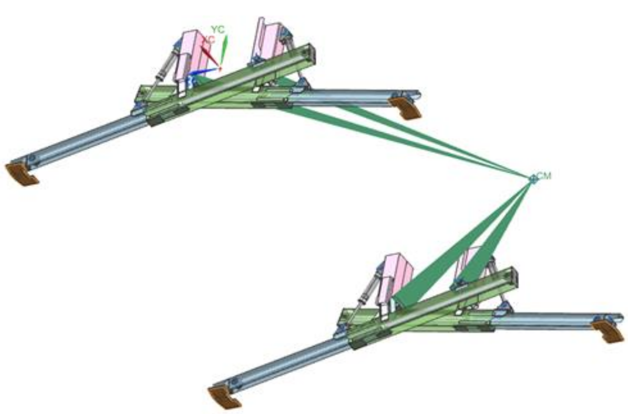

Figure 6. Simulation model limiting conditions

2.7 Material and Properties

System carrier elements consist of components such as profile, sheet metal, shaft, and bearing. In the analysis model, metal profile and sheet metal components were identified with S355 Steel, bearing components with Bronze, and shafts with AISI 4140 material. The properties of the basic materials used are shown in Table 1.

Table 1. Materials used and their main properties

Material	Type	Density (kg/m^3)	Modulus of Elasticity (Gpa)	Poisson's Ratio	Yield Strength (Mpa)
S355 Steel	Isotropic, Linear Elastic	7800	200	0.3	355
AISI 4140 Steel	Isotropic, Linear Elastic	7800	200	0.3	415
Bronze	Isotropic, Linear Elastic	8850	103.4	0.34	260

S355 steel sheet is frequently used in industry due to its low cost, high availability, ease of forming, high strength, suitable for welded and machining. In addition to the advantages of S355 steel sheets, S355 steel box sections provide product diversity with square and rectangular structures in different sizes and wall thicknesses. Thanks to their high inertia in both axes, their strength/weight ratios against axial loads are high. If the steel box section ends (outlets) are covered with a plate, the inner surfaces are easily protected from corrosion. AISI 4140 steel, on the other hand, is suitable for machining and welding processes as well as heat treatment. Therefore, it is a material frequently used in engineering applications. Bronze is a low-cost and easy-to-procure alloy that is often used in plain (sliding) bearings. Plain bearings stand out with their resistance to vibration and impacts, simple designs, easy assembly, and frequently used engineering applications.

2.8 Loading

In the single-scenario solution, since the structure's behavior under static load is examined, only 1g of gravitational acceleration is defined. In this way, the model's components and the 18-ton point mass were transformed into a static load.

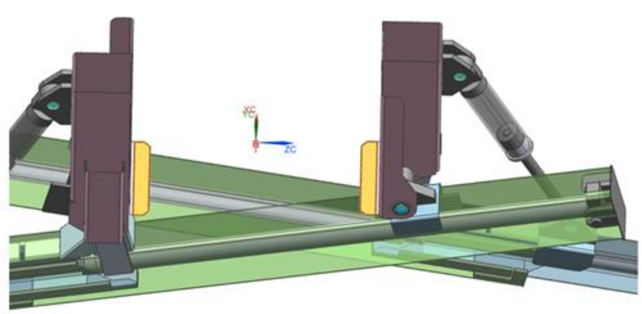

Figure 7. Load transfer interface

3. Results and discussions

In this study, the cross-type stabilizer and outriggers' design to be used on an aerial ladder firefighting vehicle was carried out, and its static analysis was performed. With the analysis performed, parameters such as displacement of the system and maximum stress were calculated, and it was evaluated whether it is suitable for prototype production.

Aerial ladder firefighting vehicle outriggers were examined in detail in the analysis program environment, and only deformation and maximum equivalent stress results were obtained for structural behavior determination in the study. An exaggerated representation is made in the visual results obtained to understand the regions with deformation more easily.

The displacement behavior of the stabilizer and outriggers in the analysis program environment was examined. Figure 8 shows the displacement results of the load application point.

According to the results obtained, the maximum displacement value of the load application point is 13-14 mm. Considering the system in general, the displacement amount is interpreted to be around 7 mm. As a result of the displacement analysis, it is concluded that the displacement is at the allowable limit value.

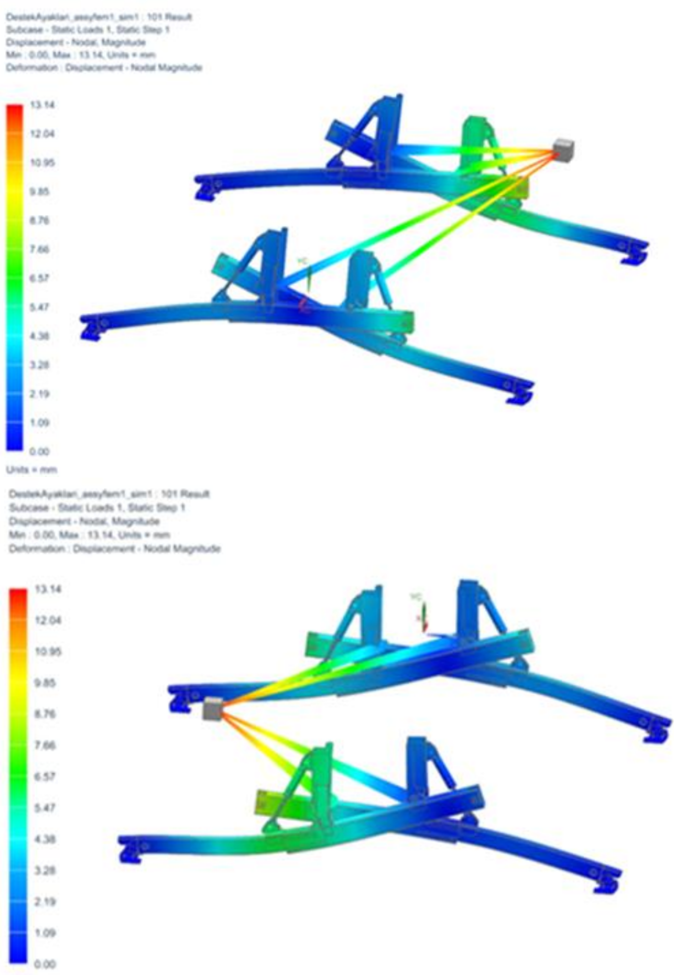

Figure 8. Rear and front view of the resulting displacement distribution

Figure 9 shows the resultant displacement results on the outriggers. According to the results, the maximum displacement on the outriggers' singular points is 4.4 and -11.78 mm. Considering the system in general, it is interpreted that the amount of displacement is around ± 4 mm. As a result of the displacement analysis, it is concluded that the displacement is at the allowable limit value.

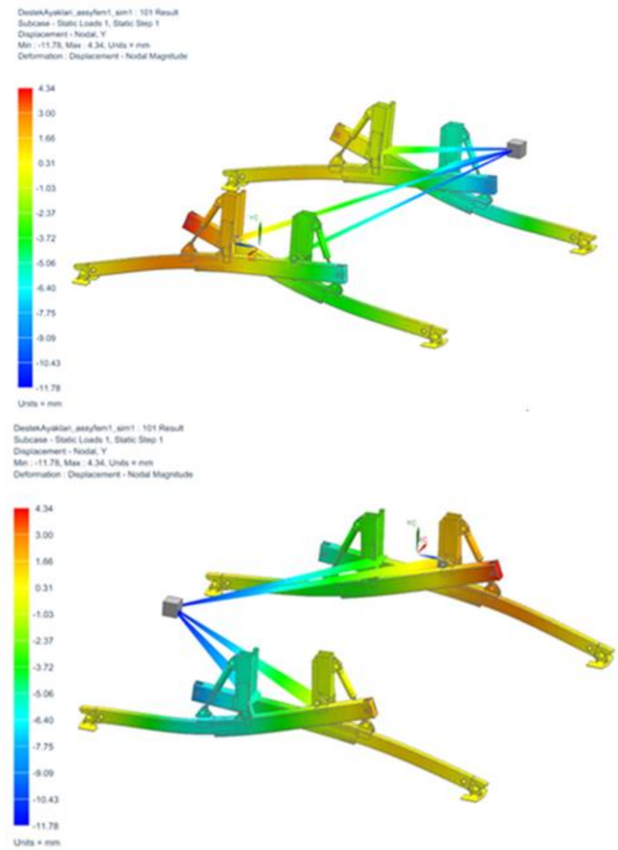

Figure 9. Y-direction displacement distribution

The stabilizer and outriggers' stress values under maximum load in the static state were examined in the analysis program environment. Figure 10 shows the stress values obtained as a result of the analysis. With reference to the yield strength of the bronze material, which has the lowest yield strength value among the materials used, the legend is limited to 260 MPa. When the stress results are examined, it is seen that the outriggers have equivalent stress values of 2500 MPa on the weld lines of the chassis connection (mounting) interfaces. These sharp edges are mathematically singular regions. These "singular" regions are formed on very short edges in the sharp geometric transition region of 2D numerical modeling elements. During the examination of the results, the values to be read from these regions do not have a physical meaning. The result is that the stress values occurring in the system are below the yield point (limit) values, except for some singular points.

The stress values of the pad region of the outriggers were examined. Figure 11 shows the equivalent stress distribution and local maximum stress values of the pad region. Because this region material is S355 JR, the legend is limited to 355 MPa. It was concluded that the stress did not exceed the yield point (limit) of the S355 JR material, except for some singular points.

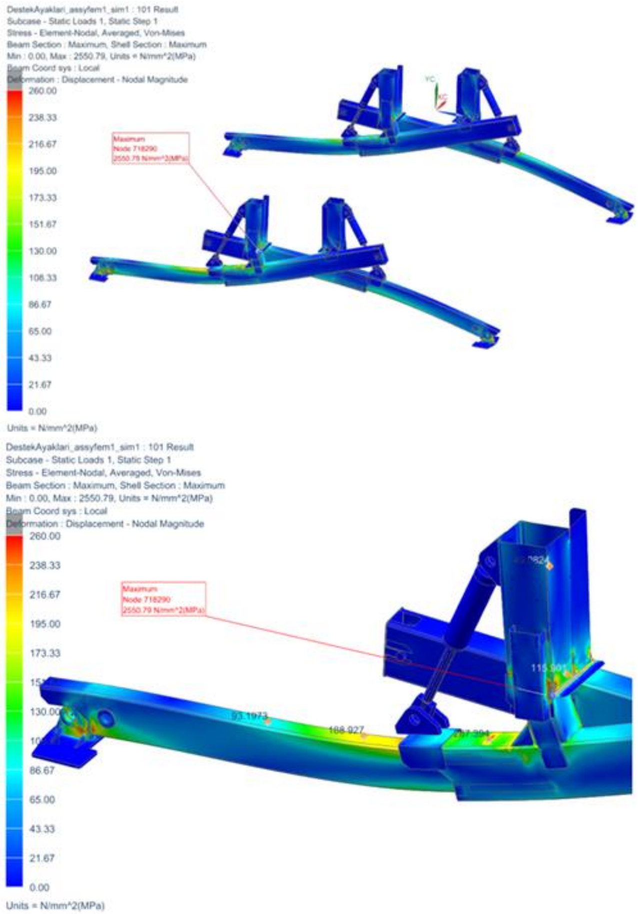

Figure 10. Equivalent stress distribution

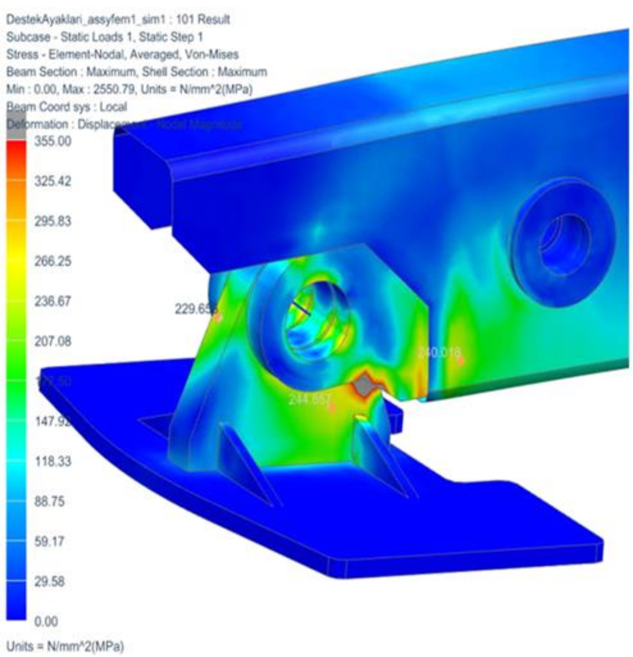

Figure 11. Equivalent stress distribution

Maximum force values affecting the shaft used in outriggers were determined in the analysis program environment. In Figure 12, it is seen that the maximum axial force on the shafts is 8138 N. The maximum axial force occurs on the front outrigger.

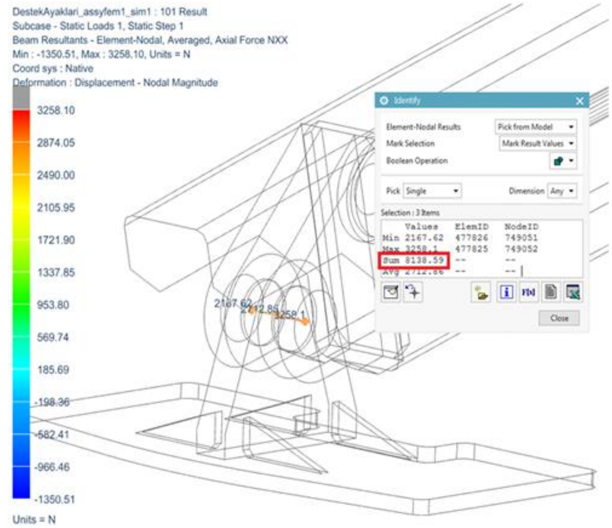

Figure 12. Maximum axial force on the front outrigger shafts

In Figure 13, it is seen that the maximum bending moment on the shafts is 226 Nm and occurs at the front outrigger. At the same time, it is seen that the maximum shear force on the shafts is 8567 N and occurs at the front outrigger.

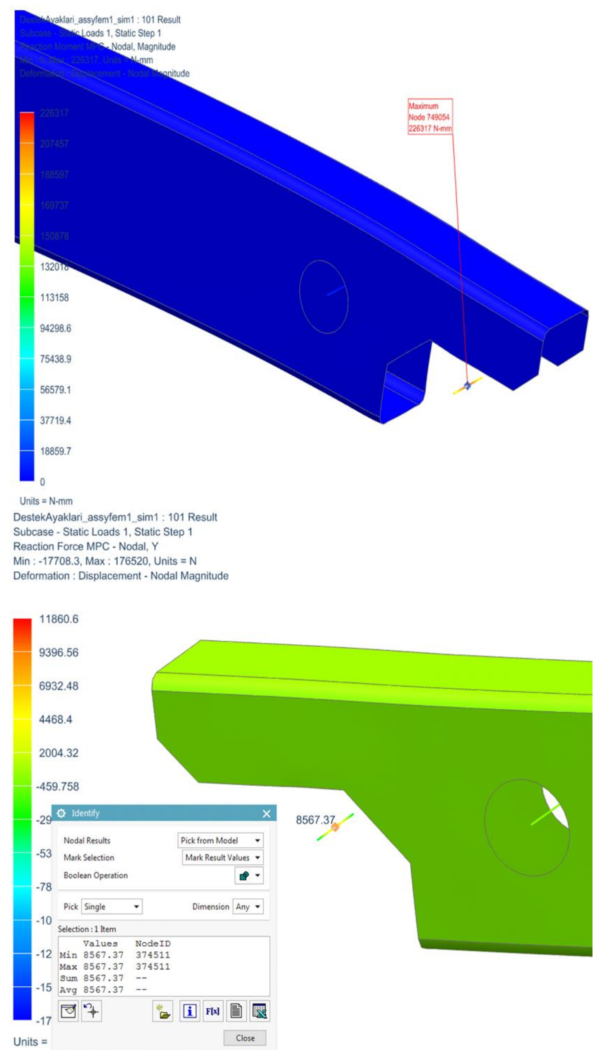

Figure 13. Maximum bending moment and shear force on shafts

Within the study's scope, the maximum loads on the connecting shafts were also calculated for the verification of the hand calculation.

According to this; the following calculations have been made.

•The maximum axial force is determined as 8138 N on the 50 mm diameter connecting rod used on the front support leg.

•The maximum bending moment was determined as 226 Nm on the 44 mm diameter front shear connecting rod.

•It has been concluded that the maximum shear force is 8567 N at the front support leg connecting rod with a diameter of 50 mm.

It has been determined that the forces acting on the shafts are well below their load-carrying capacity.

4. Conclusion

In this study, which was conducted to examine the design's resistance for the prototype production of the aerial ladder firefighting vehicle stabilizer and outrigger to the loads acting on the vehicle, the analysis results were obtained and interpreted. The results obtained for static loading cases in the analysis program environment are shown in Figures 8 to 13.

As a result of the analysis, it was seen that the load application point was displaced 13-14 mm, and the general outrigger structure was displaced approximately ± 4 mm. It is concluded that the displacement is at the acceptable (allowable) level. When the singular values are filtered, the maximum nominal stress calculated on the system is seen on the front outrigger profiles as 190 MPa (Figure 12). For this structure, which is subjected to a high degree of bending load, the maximum value location is plausible. The yield point of the profile to be produced from S355 steel material is 355 MPa. Accordingly, the system minimum factor of safety under 18 tons of loading is determined as 1.9. According to the static simulation results, it is concluded that the Outrigger design is durable (enduring) under the specified conditions.

Cross-type hydraulic outrigger and stabilizer are more ergonomic than the traditional outrigger and stabilizer type. In this study, the stresses and displacements affecting the Cross-Type Hydraulic Outrigger and Stabilizer were investigated. As a result of the examination, it was concluded that the cross-type hydraulic outrigger and stabilizer are suitable for use on the vehicle.

Conflict of Interest Statement

The authors declare that there is no conflict of interest.

CRediT Author Statement

Mustafa Karaman: Conceptualization, Supervision Analysis, Writing - review & editing, **Emre Öztürk:** Methodology, Data curation, Writing - review & editing

References

1. Senthilkumar, K., Chidanand, M., Nijalingappa, P., & Shivhare, M. M. (2010). Design, Development, and Validation of a Vehicle-mounted Hydraulically-leveled Platform. Defence Science Journal, 60(2).
2. Cuihong, Z., Xuepeng, C., Shengjie, J., Bin, Y., Guanhong, W., & Zhaoqiang, Z. (2017). A leveling mechanism for the platform based on booms-constraint control of aerial vehicle. doi:103772/jissn1006-6748201703014
3. Derlukiewicz, D., & Przybyłek, G. (2008). Chosen aspects of FEM strength analysis of telescopic jib mounted on mobile platform. Automation in construction, 17(3), 278-283.
4. Kaytukov, B., & Stepanov, M. (2018). Current Issues of Mobile Cranes Unification. In MATEC Web of Conferences (Vol. 251, p. 03011). EDP Sciences.
5. Qian, JB., Bao, LP., Yuan, RB., Yang, XJ.(2017) "Modeling and Analysis of Outrigger Reaction Forces of Hydraulic Mobile Crane", International Journal of Engineering (IJE),TRANSACTIONS B: Applications 30,8,pp.1246-1252. doi: 10.5829/ije.2017.30.08b.18
6. Stanford, N., Geng, J., Chun, Y. B., Davies, C. H. J., Nie, J. F., & Barnett, M. R. (2012). Effect of plate-shaped particle distributions on the deformation behaviour of magnesium alloy AZ91 in tension and compression. Acta materialia, 60(1), 218-228.
7. Gribniak, V., Kaklauskas, G., Kwan, A. K. H., Bacinskas, D., & Ulbinas, D. (2012). Deriving stress–strain relationships for steel fibre concrete in tension from tests of beams with ordinary reinforcement. Engineering Structures, 42, 387-395.
8. Liss, M., Kałaczyński, T., Dluhunovych, N., Dykha, A., & Martinod, R. M. (2021, January). Identification of loads of the construction of a Hybrid Multimedia Mobile Stage. In MATEC Web of Conferences (Vol. 332, p. 01024). EDP Sciences.
9. Yang, Z., Sun, Z., Jiang, S., Mao, Q., Liu, P., & Xu, C. (2020). Structural Analysis on Impact-Mechanical Properties of Ultra-High Hydraulic Support. Int. J. Simul. Model, 19, 17-28.
10. Yang, Y., Zeng, Q., Zhou, J., Wan, L., & Gao, K. (2018). The design and analysis of a new slipper-type hydraulic support. Plos one, 13(8), e0202431.
11. Lu, X., Lv, Z., & Lv, Q. (2020). Self‐centering viscoelastic diagonal brace for the outrigger of supertall buildings: Development and experiment investigation. The Structural Design of Tall and Special Buildings, 29(1), e1684.
12. Romanello, G. (2020). A graphical approach for the determination of outrigger loads in mobile cranes. Mechanics Based Design of Structures and Machines, 1-14.
13. Ali, G. M., Mansoor, A., Liu, S., Olearczyk, J., Bouferguene, A., & Al-Hussein, M. (2021). Simulation of ground bearing pressure profile under hydraulic crane outrigger mats for the verification of 16-point combined loading. Procedia Computer Science, 180, 482-491.
14. Aneziris, O.N., Papazoglou, I.A., Mudb, M.L., Damen,M., Kuiper,J., Baksteen,H., Ale,B.J., Bellamy, L.J., Hale,A.R., Bloemhoff,A., Post,J.G., Oh,J. (2008) "Towards risk assessment for crane activities", Safety Science, 46,6,pp.872-884.
15. Kan, C., Anumba, C. J., & Messner, J. I. (2019). A framework for CPS-based real-time mobile crane operations. In Advances in informatics and computing in civil and construction engineering (pp. 653-660). Springer, Cham.
16. Fang, Y., Cho, Y. K., & Chen, J. (2016). A framework for real-time proactive safety assistance for mobile crane lifting operations. Automation in Construction, 72, 367-379.
17. Hamid, A. R. A., Azhari, R., Zakaria, R., Aminudin, E., Jaya, R. P., Nagarajan, L., Yunus, R. (2019, January). Causes of crane accidents at construction sites in Malaysia. In IOP Conference Series: Earth and Environmental Science (Vol. 220, p. 012028).
18. Lee, J., Phillips, I., & Lynch, Z. (2020). Causes and prevention of mobile

crane-related accidents in South Korea. International journal of occupational safety and ergonomics, (just-accepted), 1-30.

19. Milazzo, M.F., Ancione, G., Spasojević-Brkić, V.K., Valis, D. (2017) “Investigation of crane operation safety by analysing main accident causes”, Risk, Reliability and Safety: Innovating Theory and Practice – Walls, Revie & Bedford, Taylor & Francis Group, London, ISBN 978-1-138-02997-2, pp.74-80.
20. Krastanov,K. (2017) “About the safety by usıng of mobıle cranes”, International Conference on Technology, Engineering and Science, Volume 1, pp.213-217.
21. Neitzel, R.L., Seixas, N.S., Ren,K. K. (2001) “A review of crane safety in the construction industry. Applied Occupational and Environmental Hygiene”, Applied Occupational and Environmental Hygiene 16,12, pp.1106–1117.
22. Siemens, A. G. "NX Nastran User’s Guide." Siemens Product Lifecycle Management Software Inc (2014).

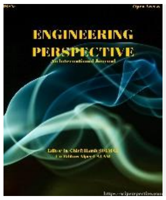

e-ISSN:2757-9077

ENGINEERING PERSPECTIVE

https://sciperspective.com/

Research Paper

Response Surface Method Based Optimization of the Viscosity of Waste Cooking Oil Biodiesel

Sedef Köse[1], Mustafa Babagiray[2*], Tolga Kocakulak[3]

[1]*Automotive Engineering Department, Faculty of Technology, Gazi University, Ankara, 06500, Turkey*
[2]*Automotive Engineering Department, Faculty of Technology, Afyon Kocatepe University, Afyonkarahisar, 03200, Turkey*
[3]*Electricity and Energy Department, Vocational High School of Technical Sciences, Burdur Mehmet Akif Ersoy University, Burdur, 15030, Turkey*

Abstract

In this study, biodiesel fuel production from waste sunflower oil and viscosity optimization was carried out. During the production process, catalyst ratio, alcohol ratio and reaction temperature were determined as variable parameters. Transesferication method was used as the production method. During the production process, the use of NaOH catalyst and methyl alcohol was provided. Biodiesel production steps with the transesterification method were discussed in detail. A total of 27 different biodiesel fuels were obtained with a catalyst ratio varying between 0.03% and 0.07%, alcohol content between 15% and 25%, and reaction temperature between 50 ° C and 70 ° C. All biodiesel fuels were analyzed and their characteristics were determined. In the optimization process, catalyst ratio, temperature and alcohol ratio were considered as input parameters, and viscosity as output parameters.Both 3D surface plots and 2D contour plots were developed using MINITAB 19 to predict optimum biodiesel viscosity. To predict biodiesel viscosity a quadratic model was created and it showed an R2 of 0.95 indicating satisfactory of the model. Minimum biodiesel viscosity of 4.37 was obtained at a temperature of 60, NaOH catalyst concentration of 0.07% and an alcohol ratio of 25%. At these reaction conditions, the predicted biodiesel viscosity was 4.247. These results demonstrate reliable prediction of the viscosity by Response surface methodology(RSM).

Keywords: Response surface methodology, biodiesel production, viscosity, waste cooking oil

History
Received: 07.02.2021
Accepted: 21.03.2021

http://dx.doi.org/10.29228/sciperspective.49697

Author Contacts
**Corresponding Author*
sedefkose22@gmail.com, mbabagiray@aku.edu.tr, tkocakulak@mehmetakif.edu.tr
Orcid: 0000-0002-1562-1403, 0000-0002-2482-6662, 0000-0002-1269-6370

1. Introduction

Due to the rapid increase in the world population and technological developments, the number of vehicles and energy need are increasing. Diesel engines are widely used in passenger and freight transportation, agricultural and industrial activities due to their high efficiency and durability [1]. These vehicles are dependent on fossil fuels to meet the energy needs [2,3]. But fossil energy sources are non-renewable energy sources. For this reason, it becomes difficult to provide it in a sustainable way and to ensure energy security [4]. Emissions from diesel engines bring negative effects along with it. This means that the exhaust emissions from vehicles will cause problems for the environment and human health [5,6]. In order to close the gap between consumed energy and produced energy and to obtain sustainable clean energy, there has been a tendency towards alternative, renewable energy sources [7,8].

An alternative fuel should be economically competitive with diesel fuel, be environmentally safe and readily available. The most important alternative fuels for diesel engines are biodiesel fuels under biomass energy [9,10]. Biodiesel fuel can be produced from vegetable, animal or marine products. In addition, biodiesel can be produced from waste oils [11,12]. Different methods are used for biodiesel production. Biodiesel production can be realized by dilution, micro-emission, pyrolysis and transesterification methods [13,14]. The method of producing biodiesel as a result of the reaction of vegetable and animal oils with alcohol is called transesterification. Transesterification method is widely used due to its low cost, mild reaction conditions, ease of production and properties close to standard diesel fuel. This method also has disadvantages such as the difficulty of separation processes, the risk of side reactions and the large amount of water waste [15,16]. There are almost no aromatic compounds, carcinogenic substances and sulfur in its structure. It can be used in standard diesel engine without any change.

Biodiesel fuel has many advantages. Biodiesel fuel has basic advantages such as no risk of extinction, supporting agricultural development, reducing foreign dependency, and being environmentally friendly. The high cetane number decreases the knock value. Its high flash point increases transport and storage safety. It is a more lubricating fuel than standard diesel fuel and reduces wear values. Besides these advantages, there are also disadvantages. Its calorific value is lower than petrol based diesel fuel. This feature causes a slight decrease in power as a result of combustion in the engine, decrease in engine performance and increase in specific fuel consumption. Its viscosity is higher than diesel fuel, it is affected more quickly by cold weather conditions. This situation is a factor limiting the use of biodiesel in engines in cold climates and in pure form [17,18,19,20].

In experimental studies, it is necessary to know the experiment design, parameters and what to expect from the test result in order to reach a correct result. Even if all these conditions are met, it may be necessary to make a large number of the same analysis or experiment. Reducing the number of experiments provides labor, time and cost savings. For this reason, a design determined with the correct parameters and levels is a reason for preference [21]. Response Surface Method (RSM) is taking its place in current statistical methods [22,23]. RSM was developed by Box and Wilson in 1951 and was first applied to the chemical industry [24]. RSM is widely used in the formulation of a new product, improvement of existing product design, process optimization, process development and improvement [25]. Response Surface Methodology can be used in experiments with at least two or more parameters. It is used for mathematical modeling and optimization of the relationship between outputs and inputs based on the results obtained from experiment combinations consisting of different levels of parameters. This method is also known as the experimental design method [21]. RSM uses experimental modeling techniques used to determine the relationship between the system's response and the independent variables affecting it. It includes experimental strategies and optimization techniques to investigate the experimental space of process variables [26].

Anwar et al., have produced biodiesel from Australian native stone fruit by transesterification method. They took methanol oil molar ratio, catalyst ratio and temperature as variable parameters to use in the production process. Both 3D surface plots and 2D contour plots were developed using MINITAB 18 to estimate the optimum biodiesel yield. After optimization for maximum biodiesel yield, they found a methanol: oil molar ratio of 6: 1, KOH catalyst ratio 0.5% and a reaction temperature of 55 C. They determined the biodiesel yield produced under these reaction conditions as 95.9% [27]. Nayak et al., examined the optimization of methyl ester yield of biodiesel fuel produced from papaya oil using response surface method. They took temperature, catalyst amount, methanol / oil molar ratio and reaction time as variable parameters. Based on the optimum condition, the predicted biodiesel yield was 99.9% and the actual experimental value was 99.3% [28]. Latchubugata et al., optimized parameters such as temperature value, reaction time and methanol / oil molar ratio used in the process of biodiesel production from palm oil with the Response surface method. They produced biodiesel fuel at the parameter values reached as a result of optimization. As a result of the analysis they applied to the produced biodiesel fuel, they found that the optimization reached the result with high accuracy [29]. The response surface method has been applied in different working areas and successful results have been achieved. Güvercin et al., using the Response Surface Method, optimized the cutting parameters that affect the surface roughness. They successfully performed the determination of the parameter and the optimum value that most affected the results obtained in the experiments [26]. Ozmetin et al., conducted an experimental study on paint chemistry and optimized the results with the Response Surface Method. With the result they achieved by optimization, they reached the targeted values [21].

In this paper, biodiesel fuel production from waste sunflower oil and viscosity optimization were carried out depending on the alcohol ratio, catalyst ratio and temperature values. In the optimization performed with the response surface method, it has been concluded that biodiesel should be produced at 66.96 ° C temperature, 0.07% NaOH catalyst ratio and 25% alcohol ratio to obtain a minimum biodiesel viscosity of 4.227.

2. Material and Method

In this study, biodiesel fuel was produced from waste sunflower oil, depending on the alcohol ratio, catalyst ratio and temperature values. Transesterification method is used in the production of biodiesel fuel. The biodiesel production process and the response surface method stages applied to the analysis results obtained were examined in detail.

2.1 Biodiesel production

Transesterification method was used for the production of biodiesel from waste sunflower oil. This method consists of 6 steps: mixing alcohol and catalyst, reaction, separation, alcohol removal, glycerin neutralization and methyl ester washing process. The stages of biodiesel production by the transesterification method can be seen schematically in figure 1 [30-34].

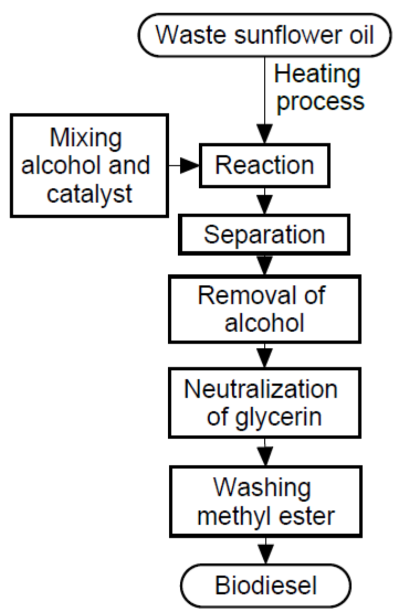

Figure 1. Biodiesel production process with transesterification method[30]

Beaker, glass bubble, cooler, density measuring device, separation funnel, heated magnetic stirrer with thermocouple, magnetic fish and precision scales were used for biodiesel production. The technical characteristics of the materials used in biodiesel production are given in table 1.

Table 1. Technical properties of materials used in biodiesel production

Material name	Waste sunflower oil	Sodium hydroxide (NaOH)	Methyl alcohol (CH_3OH)
Density (g/cm^3)	0.922	2.13	0.790-0.793
Molecular weight (g/mol)	-	40	32.04
Boiling point	-	-	64-65
Melting point	-	319-322°C	-
Resolution	1090 g/l	-	-
Refractive index	-	-	1.328-1.331

Table 2. Technical properties of viscosity device

Device Name	Brand / Model	Measuring Range	Temperature Range	Sample Volume
Viscosity	Omnitek D445	0.15-25,000 mm^2/s @ 40 °C	15-150 °C	8-16 ml

Waste sunflower oil was heated up to 80 ° C and then filtered. In order to evaporate the water molecules in the oil, it was kept at 120 ° C for about 1 hour. A homogeneous solution was prepared with NaOH catalyst and methyl alcohol and mixed with waste sunflower oil. Twenty-seven different biodiesel production was carried out, with catalyst ratio varying between 0.03% and 0.07%, alcohol content between 15% and 25%, and reaction temperature between 50 ° C and 70 ° C. The reaction time was kept constant at 1.5 hours in all production processes. The setup where the reaction taking place during the production process takes place is shown in Figure 2.

Figure 2. Reaction setup

After the reaction, the separation of glycerin from biodiesel took approximately 10 hours. The glycerin separation process in the biodiesel production process is shown in Figure 3.The fatty acids, catalysts and unreacted alcohols contained in the biodiesel obtained as a result of the reaction were removed by washing. The washing process was repeated until the fuel cleared. For this study, 5 repetitive washing processes were carried out. The washing process is shown in figure 4. After the washing process, drying and filtering process was applied to biodiesel fuel again.

Figure 3. Separating glycerin in biodiesel

Figure 4. Biodiesel fuel washing process

2.2 Design of Experiments

Response surface methodology was used for statistica analysis of the experimental data using the MINITAB 19 software. The Box-Behnken is one of the most commonly used response surface methodology designs. This design was used for statistical anaalysis and designing of this experiment. The Box-Behnken design matrix was utilised to find the optimum conditions for minimum biodiesel viscosity. The experimental optimization was achieved via ANOVA (analaysis of variance) using MINITAB 19 software. The effect of process factors such as alcohol, NaOH catalyst concentration, and temperature were tested. Using these three factors at three levels required a total of 15 runs for identifying the optimum conditions for biodiesel viscosity. The ranges, coded symbols and levels of the factors are shown in Table 3. The design matrix fort he three factors was varied at three levels, namely -1, 0 and +1.

Table 3. Range and levels coded for independent factors

Factors	Unit	Symbol Coded	Range and Levels		
			-1	0	+1
Alcohol	(%)	A	15	20	25
NaOH catalyst concentration	(%)	C	0.03	0.05	0.07
Temperature	°C	T	50	60	70

Alcohol ratio ranged from 15% to 25%, NaOH catalyst concentrations were 0.03 – 0.07% and the reaction temperature was varied from 50 °C to 70 °C. The response factor (biodiesel viscosity) was correlated to the parameters using a full quadratic model. The general form of full quadratic model is expressed as follows,

$$Y = B_0 + B_1X_1 + B_2X_2 + B_3X_3 + B_{1,2}X_1X_2 + B_{1,3}X_1X_3 + B_{2,3}X_2X_3 + B_{1,1}{X_1}^2 + B_{2,2}{X_2}^2 + B_{3,3}{X_3}^2 \quad (1)$$

where Y is the predicted biodiesel viscosity; B_0 is a constant; B_1, B_2, and B_3 are regression coefficients; $B_{1,1}$, $B_{1,2}$, $B_{1,3}$, and $B_{2,3}$ are quadratic coefficient; and X_1, X_2, and X_3 are independet variables.

3. Simulation Results

The results of the Box-Behnken design model to optimize biodiesel viscosity parameters are shown in Table 4. In the experimental results, the viscosity of biodiesel ranged from 4.376 to 5.478 mm2/s. This design matrix also show the run order, experimental viscosity values and predicted viscosity values. To avoid systematic errors, all run orders were randomised.

Table 4. Experimental matrix and Box-Behnken results

Exp. Number	Run Order	T	A	C	Temp. (°C)	Alcohol (%)	Catalyst (%)	Biodiesel Viscosity	
								Experimental	Predicted
1	5	-1	0	-1	50	15	0,05	5,058	5,00575
2	7	-1	0	1	50	25	0,05	4,518	4,53250
3	10	0	1	-1	60	15	0,07	4,627	4,56562
4	8	1	0	1	70	25	0,05	4,442	4,49425
5	6	1	0	-1	70	15	0,05	5,090	5,07550
6	4	1	1	0	70	20	0,07	4,423	4,49887
7	14	0	0	0	60	20	0,05	4,816	4,81600
8	11	0	-1	1	60	25	0,03	4,759	4,82037
9	15	0	0	0	60	20	0,05	4,816	4,81600
10	2	1	-1	0	70	20	0,03	5,478	5,36437
11	3	-1	1	0	50	20	0,07	4,453	4,56662
12	9	0	-1	-1	60	15	0,03	5,429	5,55713
13	12	0	1	1	60	25	0,07	4,376	4,24787
14	13	0	0	0	60	20	0,05	4,816	4,81600
15	1	-1	-1	0	50	20	0,03	5,341	5,26512

The predicted biodiesel viscosity values were obtained from Minitab software version 19.0 using a quadratic regression model by means of response surface methodology (RSM) analysis of experimental data. Minitab 19 program was used to calculate each parameter and the effects of their interactions with other parameters. Biodiesel viscosity was correlated with other parameters using the quadratic regression model shown in Equation (2).

$$V = 7.22 - 0.0302T - 44C + 0.059A + 0.000435T^2 + 161C^2 - 0.0033A^2 - 0.209TC - 0.00054TA + 1.047KA \quad (2)$$

Here, V is response, C is catalyst concentration, T is a reaction temperature, and A represents alcohol ratio.

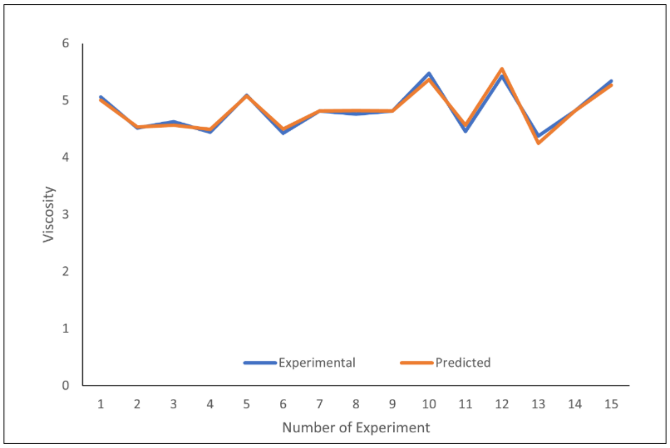

5. Experimental and RSM fitting

Comparison of experimental and predicted biodiesel are shown in Fig. 5. It is seen that there is a sufficient correlation between RSM predictive values and experimental values confirming the acceptability of the model.

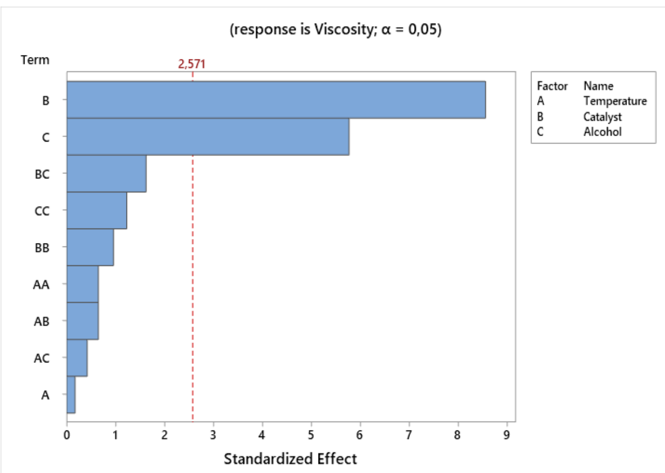

Figure 6. Effects of factors

Table 5. Regression coefficients

Term.	Coefficients	Standard Errors	T-Value	P-Value
Constant	4,8160	0,0746	64,52	0,000
T	0,0079	0,0457	0,17	0,870
C	-0,3910	0,0457	-8,55	0,000
A	-0,2636	0,0457	-5,77	0,002
$T \times T$	0,0435	0,0673	0,65	0,546
$C \times C$	0,0643	0,0673	0,95	0,383
$A \times A$	-0,0825	0,0673	-1,23	0,275
$T \times C$	-0,0417	0,0646	-0,65	0,547
$T \times A$	-0,0270	0,0646	-0,42	0,694
$K \times A$	0,1048	0,0646	1,62	0,166

In order to investigate the effects on biodiesel viscosity, linear, quadratic and interaction effects of parameters were taken into account. Table 5 and Figure 6 show the importance of these parameters in terms of the probability value (p-value). It also shows the obtained regression coefficients and calculated T-values. In the model, positive coefficients T, T2, K and KA had a positive effect on biodiesel viscosity, while A, A2, TC, TA and C had negative effects on biodiesel viscosity. Analysis of variance (ANOVA) was used to determine the importance and appropriateness of the quadratic model.

Table 6. ANOVA results for biodiesel viscosity

Source	Degree of Freedom	Sum of Squares	Mean square	F-Value	P-Value	Remarks
Model	9	1,88910	0,20990	11,22	0,008	Significant
Linear	3	1,77953	0,59318	31,71	0,001	Significant
T-Temperature	1	0,00050	0,00050	0,03	0,877	Not significant
C-Catalyst	1	1,22305	1,22305	65,37	0,000	Highly significant
A-Alcohol	1	0,55599	0,55599	29,72	0,003	Significant
Square	3	0,05580	0,01860	0,99	0,467	Not significant
T^2	1	0,01271	0,01271	0,68	0,447	Not significant
C^2	1	0,02329	0,02329	1,24	0,315	Not significant
A^2	1	0,01674	0,01674	0,89	0,388	Not significant
TC	3	0,05378	0,01793	0,96	0,480	Not significant
TA	1	0,00697	0,00697	0,37	0,568	Not significant
CA	1	0,00292	0,00292	0,16	0,709	Not significant
Lack-of-Fit	1	0,04389	0,04389	2,35	0,186	Not significant
Pure Error	5	0,09354	0,01871			
Total	3	0,08358	0,02786	5,59	0,155	
R^2=0.9575	2	0,00996	0,00498			

Table 6 shows the significance of the individual terms and their interaction on the selected response. The P value is used to check the significance of each regression coefficient by representing the error probability. The interaction effect of each cross product can be revealed through the p value[27]. It is found, C (Catalyst concentration), A (Alcohol) have significant effects on biodiesel viscosity. It is seen that C value has the lowest p value (0.000) and the highest F value (73.16) according to all other parameters. These results show that the C value is the most important parameter in biodiesel viscosity. According to the regression model in Equation (1), A has a positive effect and both C and reaction temperature (T) have negative effects on biodiesel viscosity. This implies that increasing A will increase the viscosity of the biodiesel. However, increase in C and T will decrease the viscosity of biodiesel. The ANOVA results showed that the linear term of T with p value was not significant (more than 0.05) and its quadratic term T2 with p value also was significant (more than 0.05). R2 also shows good correlation between independent parameters. In this study, R2 was found to be 95.75% and the corrected coefficient of determination (Adj. R2) was found to be 88.11%. This means that the model explains 95.75% of the variation in experimental data. As a result, the regression model developed for biodiesel viscosity was valid and showed a satisfactory experimental relationship between response and parameters.

3.1 Interaction effect of Alcohol and Temperature

The interaction effect of alcohol A and catalyst concentration, C on biodiesel viscosity in both the 3D surface plot and the contour plot are shown in Figure 3. With an increase of catalyst concentration 0.07(highest) and alcohol 25% (highest) biodiesel viscosity decrease. The minimum viscosity of biodiesel value of 4.227 mm2/s was found for NaOH 0.07 % (Run 12). Table 3 design matrix indicated that lowest NaOH concentration at 0.03% and mid-value of alcohol ratio at 20% resulted in highest biodiesel viscosity. When the Alcohol ratio remains unchanged at 25% and catalyst concentration is at lowest value of 0.03, the biodiesel viscosity decreases 4.759 mm2/s (Run 11). When the alcohol ratio was reduced to 15 % (lowest level), and with the highest value of catalyst concentration of 0.07%, the biodiesel viscosity was found to be 4.627 (Run10). Again, at alcohol ratio of 25%, and with the mid-value of catalyst concentration of 0.05%, the viscosity was found to be 4.442% mm2/s (Run 7). On the other hand, when the alcohol ratio was reduced to 15, and with the mid-value of catalyst concentration of 0.05% the yield rose up to 5.09 mm2/s (Run 6). Alcohol ratio affected total biodiesel viscosity. ANOVA from Table 6 confirmed that both A and C interaction were significant. The 2D contour plot with A and C interaction along with biodiesel viscosity is shown in Figure 7. It is easy to identify the optimum operating conditions and the related response values (viscosity) through the 2D contour plot. Therefore, both A and C are significant for lower biodiesel viscosity.

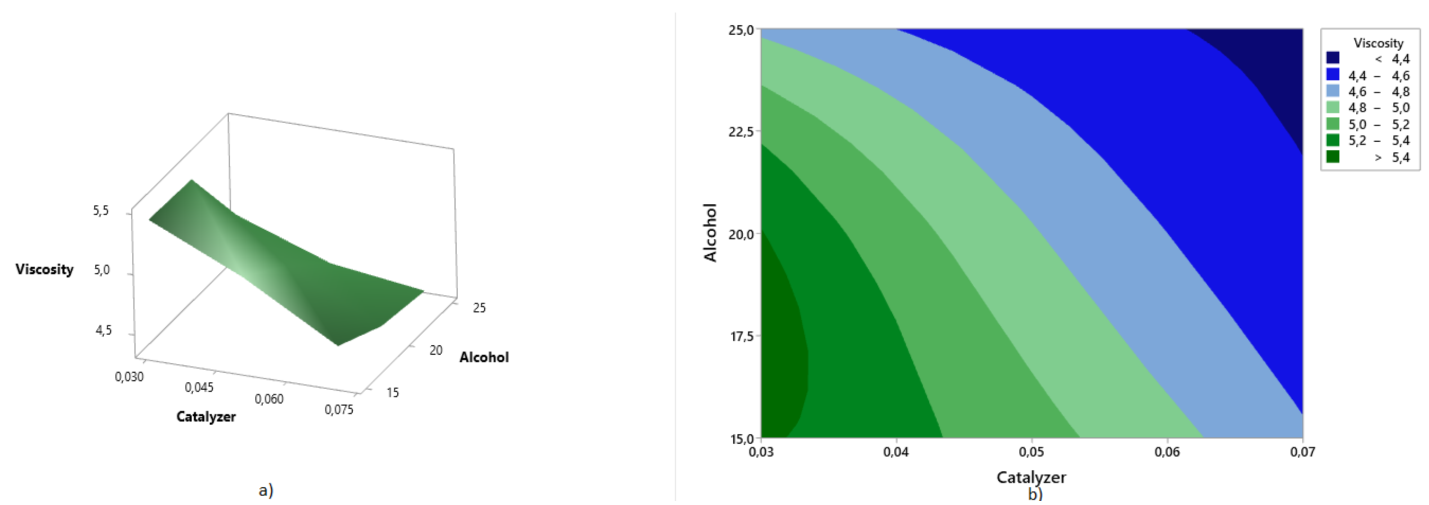

Figure 7. Interaction effect of Alcohol and catalyst concentration on bioediesel viscosity a) 3D surface plot, b) Contour plot

4. Conclusions

In biodiesel production process, catalyst ratio, alcohol ratio and reaction temperature were determined as variable parameters. Transesferication method was used as the production method. During the production process, the use of NaOH catalyst and methyl alcohol was provided. Biodiesel production steps with the transesterification method were discussed in detail. A total of 27 different biodiesel fuels were obtained with a catalyst ratio varying between 0.03% and 0.07%, alcohol content between 15% and 25%, and reaction temperature between 50 ° C and 70 ° C. All biodiesel fuels were analyzed and their characteristics were determined. A response surface methodology based on Box–Behnken design matrix was applied to achieve the optimum biodiesel viscosity. Three main parameters were changed separately at different intervals to estimate the biodiesel viscosity in this matrix. Based on the results, optimum biodiesel viscosity were found to be Alcohol ratio of 25%, catalyst concentration 0.07%, and a reaction temperature of 66.96 ◦C. The minimum biodiesel viscosity under such conditions was 4.376 mm2/s, which also confirmed the RSM model prediction of 4.227 mm2/s. ANOVA statistics of this study confirmed that catalyst concentration ratio has the most significant effect on the biodiesel viscosity, whereas reaction temperature does not seem to have any significant impact.

Nomenclature

ANOVA	Analysis of Variance
RSM	Response Surface Method

Conflict of Interest Statement

The authors declare that there is no conflict of interest.

CRediT Author Statement

Sedef Köse: Biodiesel production, methodology, article editing, **Mustafa Babagiray:** Supervision, using RSM, **Tolga Kocakulak:** Writing original draft and revision

Acknowledgements

This study was supported by AKUYAL (Afyon Kocatepe University Fuel Analysis Laboratuvary).We thank AKUYAL for their support.

References

1. Uyumaz, A., Aydoğan B., Yılmaz, E., Solmaz, H., Aksoy, F., Mutlu, İ.,Calam, A. (2020). Experimental investigation on the combustion, performance and exhaust emission characteristics of poppy oil biodiesel-diesel dual fuel combustion in a CI engine. Fuel, 280, 118588. https://doi.org/10.1016/j.fuel.2020.118588
2. Milano, J., Ong, H. C., Masjuki, H. H., Chong, W. T., Lam, M. K., Loh, P. K., Vellayan, V. (2016). Microalgae biofuels as an alternative to fossil fuel for power generation. Renewable and Sustainable Energy Reviews, 58, 180-197. https://doi.org/10.1016/j.rser.2015.12.150
3. Fooster, E., Contestabile, M., Blazquez, J., Manzano, B., Workman, M., Shah, N. (2017). The unstudied barriers to widespread renewable energy deployment: Fossil fuel price responses. Energy Policy, 103, 258-264.https://doi.org/10.1016/j.enpol.2016.12.050
4. Tietjen, O., Pahle, M., Fuss, S. (2016). Investment risks in power generation: A comparison of fossil fuel and renewable energy dominated markets. Energy Economics, 58, 174-185. https://doi.org/10.1016/j.jeem.2015.03.004
5. Kocakulak, T., Solmaz, H. (2020). Ön ve son iletimli paralel hibrit araçların bulanık mantık yöntemi ile kontrolü ve diğer güç sistemleri ile karşılaştırılması. Gazi Üniversitesi Mühendislik Mimarlık Fakültesi Dergisi, 35(4), 2269-2286. 10.17341/gazimmfd.709101.
6. Kocakulak, T., Solmaz, H. (2020). HCCI Menzil Arttırıcı Motor Kullanılan Seri Hibrit Bir Aracın Modellenmesi. Gazi Üniversitesi Fen Bilimleri Dergisi Part C: Tasarım ve Teknoloji, 8(2), 279-292. https://doi.org/10.29109/gujsc.670564
7. Sher, F., Iqbal, S. Z., Liu, H., Imran, M., Snape, C. E. (2020). Thermal and kinetic analysis of diverse biomass fuels under different reaction environment: A way forward to renewable energy sources. Energy Conversion and Management, 203, 112266. https://doi.org/10.1016/j.enconman.2019.112266
8. Chen, W. H., Ong, H., Bhaskar, T. (2020). Biomass Processing for Biofuels, Bioenergy and Chemicals. MDPI-Multidisciplinary Digital Publishing Institute.
9. Goh, B. H. H., Ong, H. C., Cheah, M. Y., Chen, W. H., Yu, K. L., Mahlia, T. M. I. (2019). Sustainability of direct biodiesel synthesis from microalgae biomass: A critical review. Renewable and Sustainable Energy Reviews, 107, 59-74.https://doi.org/10.1016/j.rser.2019.02.012
10. Quah, R. V., Tan, Y. H., Mubarak, N. M., Khalid, M., Abdullah, E. C., Nolasco-Hipolito, C. (2019). An overview of biodiesel production using recyclable biomass and non-biomass derived magnetic catalysts. Journal of Environmental Chemical Engineering, 7(4), 103219. https://doi.org/10.1016/j.jece.2019.103219
11. Olubunmi, B. E., Karmakar, B., Aderemi, O. M., Auta, M., Halder, G. (2020). Parametric optimization by Taguchi L9 approach towards biodiesel production from restaurant waste oil using Fe-supported anthill catalyst. Journal of Environmental Chemical Engineering, 8(5), 104288. https://doi.org/10.1016/j.jece.2020.104288
12. Khan, H. M., Iqbal, T., Ali, C. H., Javaid, A., Cheema, I. I. (2020). Sustainable biodiesel production from waste cooking oil utilizing waste ostrich (Struthio camelus) bones derived heterogeneous catalyst. Fuel, 277, 118091. https://doi.org/10.1016/j.fuel.2020.118091
13. Mahlia, T. M. I., Syazmi, Z. A. H. S., Mofijur, M., Abas, A. P., Bilad, M. R., Ong, H. C., Silitonga, A. S. (2020). Patent landscape review on biodiesel production: Technology updates. Renewable and Sustainable Energy Reviews, 118, 109526. https://doi.org/10.1016/j.rser.2019.109526
14. Singh, D., Sharma, D., Soni, S. L., Sharma, S., Sharma, P. K., Jhalani, A. (2020). A review on feedstocks, production processes, and yield for different generations of biodiesel. Fuel, 262, 116553.
15. Kumar, V., Thakur, I. S. (2020). Biodiesel production from transesterification of Serratia sp. ISTD04 lipids using immobilised lipase on biocomposite materials of biomineralized products of carbon dioxide sequestrating bacterium. Bioresource technology, 307, 123193. https://doi.org/10.1016/j.biortech.2020.123193
16. Toldrá-Reig, F., Mora, L., Toldrá, F. (2020). Developments in the use of lipase transesterification for biodiesel production from animal fat waste. Applied Sciences, 10(15), 5085. https://doi.org/10.3390/app10155085
17. Aksoy, F., Akay, F., Baydır, Ş. A., Solmaz, H., Yılmaz, E., Uyumaz, A., Calam, A. (2019). An Experimental Investigation on The Effects of Waste Olive Oil Biodiesel on Combustion, Engine Performance and Exhaust Emissions. International Journal of Automotive Engineering and Technologies, 8(3), 103-116. https://doi.org/10.18245/ijaet.578227
18. Gülüm M., 2014, Experimental investigation of the effects of various production parameters on the some fuel properties of produced biodiesels from corn and hazelnut oils, Master Thesis, Karadeniz Technical University Institute of Science, Trabzon.
19. Nişancı S., 2007, Experimental Investigation of the Effects of Biodiesel Fuel Blends on Performance and Emission, Master Thesis, Yıldız Technical University Institute of Science, Istanbul.
20. Pulyaeva, V. N., Kharitonova, N. A., & Kharitonova, E. N. (2020, December). Advantages and Disadvantages of the Production and Using of Liquid Biofuels. In IOP Conference Series: Materials Science and Engineering (Vol. 976, No. 1, p. 012031). IOP Publishing. doi:10.1088/1757-899X/976/1/012031
21. Özmetin, C., Özmetin, E., Süzen, Y., Fil, B. A. Optimizing Adsorption Of Methyl Violet Dye By Activated Carbon Using Response Surface Methodology. Çevre Bilim ve Teknoloji, 1.
22. Öztürk, Z. B., Nuran, A. Y. (2012). Yanıt yüzey metodu ile porselen karo küçülmesinde ergiticilerin optimizasyonu, Journal of Engineering

and Architecture Faculty of Eskişehir Osmangazi University, 25(2), 57-65.

23. Öney, Ö., Samanlı, S. (2017). Kütahya/Altıntaş grafitlerinin kaba flotasyon parametrelerinin box-behnken deney tasarımı kullanılarak optimizasyonu ve modellenmesi, Dokuz Eylul University-Faculty of Engineering Journal of Science and Engineering, 19(56), 532-542. Doi: 10.21205/deufmd. 2017195651
24. Koç, B., Kaymak-Ertekin, F. (2010). Yanıt yüzey yöntemi ve gıda işleme uygulamaları, Gıda Dergisi, 35(1), 1-8.
25. Kılıçkap, E., Hüseyinoğlu, M. (2010). Tepki yüzey modeli ve genetik algoritma kullanılarak AISI 316'nın delinmesinde oluşan çapak yüksekliğinin modellenmesi ve optimizasyonu, Dicle Üniversitesi Mühendislik Fakültesi Dergisi, 1(1), 71-80.
26. Güvercin, S., Yildiz, A. (2018). Optimization of cutting parameters using the response surface method. Sigma Journal of Engineering and Natural Sciences, 36(1), 113-121.
27. Anwar, M., Rasul, M. G., Ashwath, N., Rahman, M. M. (2018). Optimisation of second-generation biodiesel production from Australian native stone fruit oil using response surface method. Energies, 11(10), 2566. https://doi.org/10.3390/en11102566
28. Nayak, M. G., & Vyas, A. P. (2019). Optimization of microwave-assisted biodiesel production from Papaya oil using response surface methodology. Renewable Energy, 138, 18-28. https://doi.org/10.1016/j.renene.2019.01.054
29. Latchubugata, C. S., Kondapaneni, R. V., Patluri, K. K., Virendra, U., & Vedantam, S. (2018). Kinetics and optimization studies using Response Surface Methodology in biodiesel production using heterogeneous catalyst. Chemical Engineering Research and Design, 135, 129-139.
30. Sedef, Köse., Aylanşık, G., Babagiray, M., Kocakulak, T. Biodiesel Production from Waste Sunflower Oil and Engine Performance Tests. International Journal of Automotive Science and Technology, 4(4), 206-212. https://doi.org/10.30939/ijastech..770309
31. Hamze, H., Akia, M., & Yazdani, F. (2015). Optimization of biodiesel production from the waste cooking oil using response surface methodology. Process Safety and Environmental Protection, 94, 1-10.
32. H. Solmaz et Al. , "Balık İç Atıklarından Piroliz Yöntemi İle Yakıt Üretimi Ve Egzoz Emisyon Değerlerinin İncelenmesi," 14th International Combustion Sysmposium (INCOS2018) , Karabük, Turkey, 2018
33. Ramachander, J., et al. "Performance and emission predictions of a CRDI engine powered with diesel fuel: A combined study of injection parameters variation and Box-Behnken response surface methodology based optimization." Fuel 290 (2021): 120069.
34. Ashok, B., Jeevanantham, A. K., Prabhu, K., Shirude, P. M., Shinde, D. D., Nadgauda, N. S., & Karthick, C. (2021). Multi-objective optimization on vibration and noise characteristics of light duty biofuel powered engine at idling condition using response surface methodology. Journal of Energy Resources Technology, 143(4).